Oscar Hieronimus Rønning Langfoss
Simen Kvalvåg Navestad
Ivar Andre Sande

Comparative Study of Conductive Carbons' Effect on Rate Performance of LiFePO4 Cathodes in Lithium Ion Batteries

Bachelor's thesis

NTNU

Norwegian University of
Science and Technology

Oscar Hieronimus Rønning Langfoss
Simen Kvalvåg Navestad
Ivar Andre Sande

Comparative Study of Conductive Carbons' Effect on Rate Performance of LiFePO4 Cathodes in Lithium Ion Batteries

NTNU
Norwegian University of
Science and Technology

NTNU
Kunnskap for en bedre verden

Comparative Study of Conductive Carbons' Effect on Rate Performance of LiFePO4 Cathodes in Lithium Ion Batteries

Authors:
Oscar H.R. Langfoss
Simen K. Navestad
Ivar A. Sande

Supervisors:
Ann Mari Svensson
Kjersti Kleveland
Ragnhild Å. Reite
Charles D. Amos

Client:
FREYR

NTNU

Kunnskap for en bedre verden

INSTITUTT FOR MATERIALTEKNOLOGI

TMAK3001 - BACHELOROPPGAVE

Sammenligning av effekten til ledende karbon på ytelse av LiFePO4-katoder i litium-ionbatterier

Forfattere:
Oscar H.R. Langfoss
Simen K. Navestad
Ivar A. Sande

Veiledere:
Ann Mari Svensson
Kjersti Kleveland
Ragnhild Å. Reite
Charles D. Amos

Oppdragsgiver:
FREYR

Preface

This Bachelor thesis is a project provided by FREYR Battery and was carried out at the Department of Materials Science and Engineering (IMA) at NTNU.

<div align="right">

Ivar Andre Sande
Simen Kvalvåg Navestad
Oscar Hieronimus Rønning Langfoss

Trondheim
May, 2023

</div>

In a lab, a study took place,
Carbon's impact they aimed to trace.
C45 and KB,
Showed promise, they'd see,
But SFG couldn't keep up the pace.

Abstract

The aim of this comparative study was to investigate and compare different conductive carbons' effect on rate performance of LiFePO$_4$ (LFP) cathodes in lithium ion batteries. Methods for producing LFP cathodes, assembling LFP coin cells and cycling testing were made and tried. The three conductive carbon blacks investigated were SUPER C45 (C45), Ketjenblack (KB) and SFG15L (SFG). They were found to have BET surface areas of 45, 1332 and 9 m^2/g, respectively. From XRD analysis, C45 and KB exhibited amorphous and highly amorphous microstructures, while SFG displayed a highly crystalline profile.

A formulation for cathode production was found and used. A solid content of 40% for C45 and SFG, and 30% for KB was needed to make the slurries suitable for casting and made the cathode compositions comparable. These solid contents gave rise to mass loadings of 6.3, 4.5 and 6.6 mg/cm^2 for C45, KB and SFG, respectively. A standard and reproducible way of assembling coin cells was used. An appropriate CCCV cycling protocol for rate performance was structured based on the theoretical capacity of LFP and the mass loading of each sample. A current limiting step of 30% was set in relation to the C-rates of each sample.

The coin cells were rate tested at the C-rates; C/10, C/3, C/2, 1C, 2C and 5C. As a capacity retention step, a second C/3 step was used. The KB cells obtained slightly higher discharge capacities at all rate performance steps, except 2C, where the C45 cells slightly outperformed the KB cells. The SFG cells obtained comparably worse rate performance results for all C-rates. The C45 and KB cells retained 85% and 74% of their capacity through the two rates of C/3, while the SFG cells had non-applicable capacity retention results.

From analysis of the rate performance results, it was found that the conductive carbons C45 and KB made for acceptable additives in LFP cathodes. This was speculated to be due to their amorphous structure which gave rise to branching electrical pathways and great electronic conductivity. The KB cells performed worse in some rate performance metrics, and this was thought to be because of its high surface area which decreased the pore volumes within the cathode, which disturbed the electrolyte distribution and thereby decreased the ionic conductivity. SFG was found to not be a suitable conductive additive in LFP cathodes, due to its poor rate performance, fostered by its low surface area.

Sammendrag

Målet med denne studien var å undersøke og sammenligne ulike ledende karbons effekt på ytelsen til LiFePO$_4$ (LFP)-katoder i litium-ionbatterier. Metoder for å produsere LFP-katoder, sette sammen LFP-knappceller og syklisk testing ble laget og prøvd. De tre ledende karbonene som ble undersøkt var SUPER C45 (C45), Ketjenblack (KB) og SFG15L (SFG). De ble målt til å ha et BET-overflateareal på henholdsvis 45, 1332 og 9 m^2/g. Fra XRD-analyse viste C45 og KB seg å ha amorfe og svært amorfe mikrostrukturer, mens SFG hadde en svært krystallinsk profil.

En oppskrift for produksjon av katoder ble utviklet og brukt. Det var nødvendig med et fast-stoffinnhold på 40 % for C45 og SFG, og 30 % for KB for å gjøre slurryene egnet for "casting" og gjøre dem sammenlignbare. Dette ga opphav til "mass loading"-verdiene 6,3, 4,5 og 6,6 mg/cm^2 for henholdsvis C45, KB og SFG. En standard og reproduserbar måte å sette sammen knapp-celler ble funnet og brukt. En passende CCCV-syklusprotokoll for "rate performance" ble struk-turert basert på den teoretiske kapasiteten for LFP og mass loading-en til hver prøve. Et strømbegrensende trinn på 30 % ble valgt i forhold til C-ratene for hver prøve.

Knappcellene ble "rate"-testet ved C-ratene; C/10, C/3, C/2, 1C, 2C og 5C. Til slutt ble et trinn med C/3 brukt som et "capacity retention"-trinn. KB-cellene oppnådde litt høyere utlad-ningskapasitet ved alle ytelsestrinn, bortsett fra 2C, hvor C45-cellene ytet litt bedre enn KB-cellene. SFG-cellene oppnådde dårligere ytelsesresultater for alle C-rater, sammenlignet med de to andre. C45- og KB-cellene beholdt 85 % og 74 % av kapasiteten mellom de to ratene på C/3, mens SFG-cellene hadde ikke-anvendbare kapasitetsbevaringsresultater.

Analyse av ytelsesresultatene viste at de ledende karbonene C45 og KB er akseptable som tilset-ningsstoffer i LFP-katoder. Dette ble spekulert i å skyldes deres amorfe struktur som ga op-phav til forgrenede elektriske forbindelser og høy elektronisk ledningsevne. KB-cellene presterte dårligere i enkelte ytelsesmålinger. Dette ble antatt å være på grunn av KB-pulverets høye over-flateareal som reduserte det indre porevolumet i katoden. Dette kan ha begrenset fordelingen av elektrolytt og dermed redusert den ioniske ledningsevnen. Det ble også funnet at SFG ikke er et passende ledende tilsetningsstoff i LFP-katoder. Dette ble begrunnet i cellenes dårlige ytelse, noe som mulig kan forklares av pulverets svært krystallinske mikrostruktur og lave overflateareal.

LIST OF ABBREVIATIONS

Term	Description
AM	Active Material
BET	Brunauer–Emmett–Teller
CC	Constant Current
CCCV	Constant Current Constant Voltage
CE	Coulombic Efficiency
CR	Capacity Retention
CV	Constant Voltage
DEC	Diethyl Carbonate
EC	Ethylene Carbonate
GCPL	Galvanostatic Cycling with Potential Limitation
LFP	Lithium Iron Phosphate
LIB	Lithium Ion Battery
ML	Mass Loading
NMP	N-Metyl-2-Pyrrolidon
OCV	Open Circuit Voltage
PCGA	Potentiodynamic Cycling with Galvanostatic Acceleration
PVDF	Polyvinyldene Fluoride
SC	Solid Content
SEI	Solid Electrolyte Interface
SOC	State of Charge
XRD	X-Ray Diffraction

List of Figures

List of Tables

Contents

1 Introduction

1.1 Motivation

Modern society has become dependent on the lithium-ion battery (LIB) for many different applications. It enabled the wireless revolution of cell phones, laptop computers and digital cameras, and is now at the forefront of replacing the internal combustion engine by powering vehicles electrically. Can this technology enable a sustainable energy supply for all people and reduce our collective greenhouse gas emissions? Since LIBs are the conventional choice for portable electrochemical energy storage, improving their cost and performance is important to expand their applications and enable new technologies that depend on energy storage. Electrodes with higher rate capability and charge capacity can improve the energy and power densities of LIBs and make them smaller and cheaper [1]. By efficiently storing electrical energy generated by renewable sources, such as wind and solar, LIBs can relieve the power grid of unwanted fluctuations by use of stationary power stations.

For larger technology applications, e.g. within transportation and grid networks, LIBs are still costly. Shortage of lithium and other transition metals used in LIBs can become a problem in the future. The earth's crust does contain enough lithium to power a global fleet of automobiles, but the problem in Europe lies mainly within material mass import and non-existent lithium recycling [2]. Therefore, optimising the usage rates and life cycles of LIBs can have a huge influence on Europe's power demand.

1.2 Aim of work

The purpose of this study was to determine how the surface area and physical attributes of conductive carbons, when dispersed in an LFP cathode, affect the rate performance using galvanostatic cycling. To achieve this, a specific method of operations for characterising, making and testing the battery cells had to be found. To begin with, a combination of powder characterisation methods, which could purposefully give the necessary information on the carbon's morphology was identified. Then, a method of structurally and precisely constructing each cathode and cell in a way such that the carbons could be comparably tested, was required. Lastly, appropriate testing protocols and conditions which would not give rise to unwanted differentiating factors, were developed. Summarised, the methods of operations which where needed to be established to achieve the aim of work were:

1. Identify the required powder characterisation techniques
2. Develop a good cathode slurry formulation that will ensure good foundation for carbon comparison
3. Develop a testing protocol that can identify the differences in rate performance of the different cathode compositions

2 Theory

2.1 Lithium-ion: introduction and history

When SONY studied the possibilities of secondary lithium batteries in the 1980s, a lithium metal anode was proposed. It showed great potential with a high energy density as compared to other secondary battery options. However, practical usage problems were quickly discovered. The batteries exhibited poor safety characteristics, could not survive long cycling and required a long charging time. And so, alternative lithium storing anode materials was studied, to address these weaknesses. [3]. Today, a commercial full-cell LIB's anode material is often carbon graphite [4]. Graphite is used because of its well-known layered structure, which can be intercalated or doped with different ions, e.g. lithium. So, when charging a LIB, lithium doping or intercalation occurs within the graphite anode, and during discharge, the Li^+-ions are deintercalated from the anode. When not including a lithium-based anode, a lithium containing compound must be found elsewhere in the battery as a Li^+-ion source. This is where different cathodes containing lithium are used [3]. A schematic of the charging/discharging process of a LIB is presented in Figure 2.1.
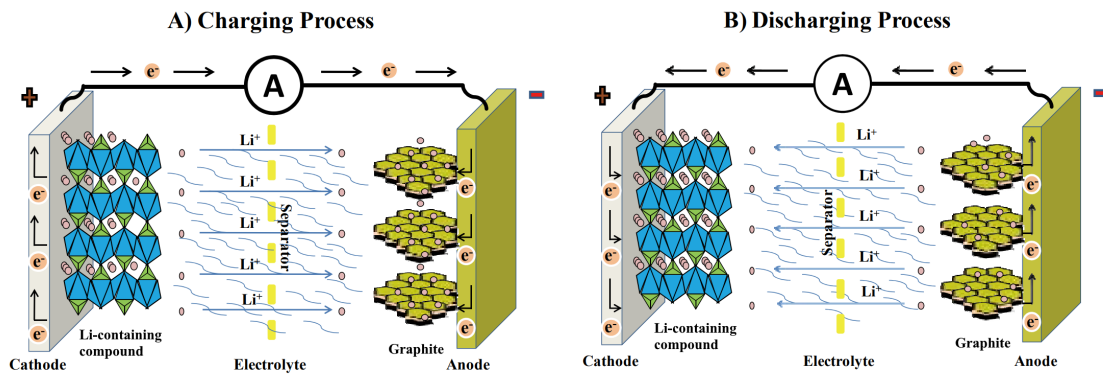
Figure 2.1: Composition of a Li^+-ion full-cell during its charging and discharging processes. Figure based on Toprakçı et. al. [5].

When categorising different types of LIBs, the electrode material compositions, are primary differentiating factors. Further, to evaluate and compare LIBs, there are an array of varying parameters used. Performance of a LIB can be evaluated with parameters such as volumetric energy, specific energy, specific capacity, charge/discharge rates, cyclability and safety [4]. When commercially presenting LIBs, a metric widely used is the specific energy or the energy density [6]. It measures the amount of energy which can be stored and released per unit mass of the battery, denoted in Wh/kg. In electric cars, energy density is an important metric, because the car battery needs to be able to store lots of energy while still being light.

Energy density is related to the specific capacity of a cell through the battery's operating voltage [4]. The specific capacity measures the battery cell's ability to reversibly store charge per unit mass and is often denoted in mAh/g. Because of the many charge/discharge cycles a LIB has to endure throughout its life time, cyclability becomes an important evaluating metric. It is measured through the number of charge/discharge cycles until the battery's energy output notably decreases or until the battery no longer can provide the required energy output [4]. In relation to cyclability, the rate performance of a LIB is often reported as useful data. This metric evaluates the capacity during different levels of current loading. Higher rate performance is usually desired [7]. As an example, in electrical vehicles, a high discharge rate is necessary, because rapid acceleration demands high discharge rates to extract lots of energy in a short amount of time. Further parameters studied during rate performance analyses are usually Coulombic efficiency (CE) and capacity retention (CR). CE is used to effectively gauge the internal reactions influencing battery life and performance. It is defined as the relation between the measured discharge capacity ($C_{dis(n)}$) and the measured charge capacity ($C_{char(n)}$), of cycle n [8]. Equation (1) presents the calculation of CE. CE is often denoted as a percentile and in an ideal cell with close to no side reactions the CE should be near 100%. A reduced CE, often leads to an exponential decline in cell cycle life and stability [9].

$$CE = \frac{C_{dis(n)}}{C_{char(n)}} \tag{1}$$

Further, CR is determined as the measured discharge capacity of a cycle ($C_{dis(n+m)}$) divided by the discharge capacity of a previous cycle ($C_{dis(n)}$). A calculation of CR can be seen in Equation (2). This gives an indication of the capacity retained between the cycles chosen. CR is also usually presented as a percentile.

$$CR = \frac{C_{dis(n+m)}}{C_{dis(n)}} \tag{2}$$

2.2   Electrodes

In conventional LIBs, electrodes typically consist of material compounds. This means that there are many possible configurations of LIBs with their own strengths and weaknesses [1]. Together with different conductive additives and current collectors, the electrode composition creates an array of different interchangeable parameters which can determine the performance, weight, and price of a LIB. Electrode materials can be categorised as either intercalation materials or conversion materials [1].

2.2.1 Intercalation materials

An intercalation material acts as a host network that stores guest ions. The guest ions are inserted into and removed from the host network reversibly, without structural changes in the host material. In a LIB, Li^+ is the guest ion and the host network compounds are often transition metal oxides or polyanion compounds. Some common intercalation materials are: lithium cobalt oxide (LCO), lithium manganese oxide (LMO), nickel manganese cobalt oxide (NMC), nickel cobalt aluminium oxide (NCA), lithium cobalt phosphate (LCP), lithium iron phosphate (LFP), lithium iron flourosulfate (LFSF) and lithium titanium sulfide (LTS) [1].

Transition metal oxides are represented by the well established $LiCoO_2$ (LCO) compound, introduced by J. B. Goodenough in 1980 [10]. The guest-host reaction of LCO can be expressed through Equation (3).

$$Li_xCoO_2 \rightleftharpoons xLi^+ + xe^- + CoO_2 \tag{3}$$
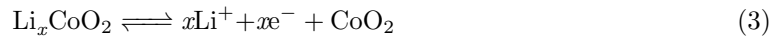
LCO has a high theoretical and volumetric capacity, low self-discharge, high discharge voltage, and good cycling performance. The downsides of LCO are high material costs, low thermal stability and fast capacity fade at high current rates or during deep cycling. Thermal stability refers to the exothermic release of oxygen when a lithium metal oxide cathode is heated above a certain point, resulting in a runaway reaction in which the cell can burst into flames [1]. Despite safety concerns, LCO has had great commercial success in the past, being widely used in the EV industry [11].

The polyanion compounds exhibit the ion structure: $(XO_4)^{3-}$, where X can be sulphur (S), phosphorus (P) or silicon (Si). These bulky anions largely occupy the lattice positions, which increases the cathode redox potential while also stabilising its structure. One common and commercially successful polyanion compound is $LiFePO_4$ (LFP). LFP has an olivine structure where Li^+ and FeO_6 occupy octahedral sites, while PO_4 is positioned in tetrahedral sites, causing a slightly distorted HCP (hexagonal closed-packed) oxygen array [1]. An illustration of the olivine structure is presented in Figure 2.2.
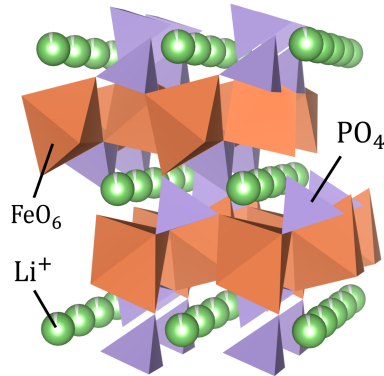
Figure 2.2: The olivine structure of LFP. Illustration created with VESTA [12] and derived from the Crystallography Open Database (COD).

LFP has good thermal stability and high power capability, but in comparison to other intercalation compounds, it has low average potential and low electrical and ionic conductivity [1]. To combat this, some performance enhancing methods have been developed, e.g. reduction of particle size and addition of a conductive carbon coating on the current collector. Another method is to integrate a conductive additive within the cathode material [1].

2.2.2 Conversion materials

For conversion cathode materials, there is no host or guest material. A solid-state redox reaction occurs inside the electrode [13]. During lithiation and delithiation, the chemical bonds are repeatedly broken and recombined. This reversible reaction usually takes form as seen in Equation (4).

$$MX_c + bLi \rightleftharpoons M + cLi_{(b/a)}X, \tag{4}$$
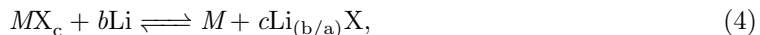
where M is a voluntary suitable metal and X is a suitable halide (F, Cl, Br, I). There are many types of conversion materials, but metal fluorides and chlorine compounds provided the highest theoretical capacities so far[1] [13]. Batteries with conversion cathode materials are typically used in hybrid car batteries [14].

2.2.3 The inner workings of electrodes and how to optimise them

An electrode's composition, structure and solid electrolyte interphase (SEI) are essential factors for controlling charge transfer processes and electrochemical performance in a LIB. Battery metrics like rate performance, Coulombic efficiency (CE) and capacity retention (CR) are largely affected by the electrode's internal charge transport system [15]. The internal flow of ions and electrons is referred to as charge transport. When trying to achieve high energy density, high power density and long cyclability of a battery, it is this charge transport system that should be optimised and rationally designed [16]. Y. Wang et. al. categorises the charge transport system of positive electrodes into four parts;

1: The ion transport network, which is controlled by the porous structure in the electrode compound,

2: The electron transport network, constructed by the conductive additive and binder,

3: The ion/electron transport within the active material, and

4: The interface between the conductive agents (conductive additives and electrolyte) and the active material [16].

These four parts are not isolated processes, and the connection between each can represent primary interfaces between the main components in an electrode. Every part interacts with and affects each other and the connection of two parts can be the dominant or limiting factor in the charge transport system.

The efficiency of the electrode charge transport system is affected by many factors. It can be difficult to point out the most important one, as they can shift with different operating conditions, but some primary categories can be established [16]. The first, and most critical, are the material factors. These include the individual conductivities of the components and their shape, size and structure, i.e., the material's morphology. The second, and most complex, are the interface factors. These factors originate from the incompatibility of the electrode components, which creates complicated interfaces. Some of these interfaces include the SEI and the conductive additive/active material interface. The third category describes the conductive network structure. The configurations of these networks fundamentally determine the charge transport capability through the 3D structures of charge pathways [16].

2.2.4 Electrode capacity

The theoretical capacity (Q_{th}) of an electrode material is calculated with respect to the relation between number of electrons transferred in the total reversible reaction of the active material (n), times the Faraday's constant (F) and the total molar mass (Mm) of the active material. An example of such a calculation is presented in Equation (5) for the active material LFP. The theoretical capacity of LFP can be approximated to 170 mAh/g. In practice, the measurement of specific capacity is always affected by the other components in the cell, therefore, the practical capacity is always less than the theoretical. [4].

$$Q_{t\,(LFP)} = \frac{n \cdot F}{M_{mLi} + M_{mFe} + M_{mP} + (4 \cdot M_{mO})} \tag{5}$$

To correctly balance the units in Equation (5), Faraday's constant must be expressed in mAh/mol. Such a calculation is done in Equation (6).

$$1\ \text{Faraday} = \frac{96485\ [\text{Cmol}^{-1}] \cdot 1000}{3600\ [\frac{s}{h}]} = 26801\ [\frac{mAh}{mol}] \tag{6}$$

The total reversible reaction of LFP is expressed in Equation (7). When a current is applied, the Li^+-ion separates from the $FePO_4$ compound, and one electron is transferred.

$$LiFePO_4 \rightleftharpoons FePO_4 + Li^+ + e^- \tag{7}$$
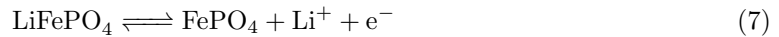
2.3 Conductive additives in LFP

LFP is among the cathode materials with the lowest conductivity [1]. Therefore, conductive additives are introduced into the cathode film. The additives form an electronic network between the active material and the current collector, which increases electronic conductivity. A good choice of conductive additive increases the conductivity, cycling life and rate capability of the cathode [17]. Carbon blacks are typically chosen as conductive additives in intercalation cathodes, as their high surface area and low cost make them great candidates for this application.

2.3.1 Characteristics of conductive carbon

Carbon black consists of near spherical primary particles of elemental carbon [18]. It is produced as soot from either thermal decomposition or partial combustion of hydrocarbons, with oil or natural gas as the raw material. There are two main manufacturing processes for obtaining this in industry, i.e., the furnace black and acetylene black process. The most common method is the furnace black process. Here, petroleum oil or coal is partially combusted by blowing the raw material into high temperature gases. This allows for wide control over material properties such as particle size and structure. In the acetylene manufacturing process, carbon black is obtained by thermally decomposing acetylene gas. The process provides a carbon product with higher structures and higher crystallinity, and is mainly used for electrically conductive agents [19] [20]. In the manufacturing process, the primary particles, or nodules, are fused together in aggregates. Nodule sizes range between 10-100 nm. The aggregates are the basic unit of carbon black, and the degree of aggregation dictate the morphological properties within the material. Aggregate sizes typically range from 100 nm to 1 µm. Clusters of aggregates form agglomerates, which are held together by weak van-der-Waals forces [21]. Agglomerates can be broken under mechanical stress, while aggregates cannot [22]. In Figure 2.3, the distinctions of carbon black particles are shown.

Primary particle   Aggregate   Agglomerate
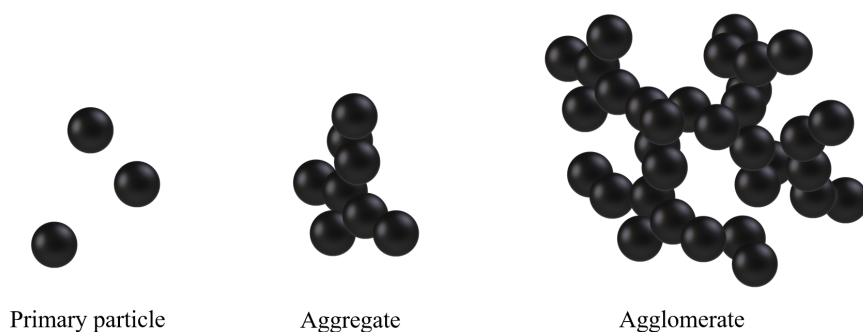
Figure 2.3: The three distinctions of carbon black particles

To distinguish between different carbon blacks, two main properties are used: the complex property of "structure" and the specific surface area. The degree of aggregation determines what is commonly known as "structure". The structure of a carbon black is the measurement of the empty space between randomly packed aggregates [22], which is determined by the number of primary particles comprising an aggregate and the way they are morphologically fused together [21]. Structure can be further categorised as grades of low or high graphitic character, which is in relation to how closely the structure of the carbon black resembles a graphite surface [18]. With high structure, the aggregates grow larger and more complex and the empty space between the aggregates increases. The opposite is valid for low grade structures. To experimentally measure the structure of carbon black, dibutyl phtalate (DBP) and oil absorption are commonly done [18]. The specific surface area represents the area of carbon black per gram of exposed material [22]. There are several methods to determine the specific surface area of a material, and for carbon black, most of them rely on adsorption isotherms [20]. The adsorption of iodine, I_2, was a fast and reliable method in early days, but was later found to inaccurate data because of surface oxidation reactions with the carbon [23]. Adsorption of nitrogen is widely used today, through BET analysis. [20].

Extent of electron transport determines the conductivity of a material, and the conductive properties of carbon black are highly influenced by the structure and surface area. For carbon black, the biggest obstacle of electron transport resides the interface between aggregates [24]. In an LFP/carbon cathode, X. Qi et al. [21] found that there is a conductivity trade-off between small carbon black particles with high surface area and bigger carbon black particles with lower surface area. Their results indicate that carbon blacks with high surface area increase the electrical contact area between the particles of the active phase (LFP) and the conductive additive, resulting in an increase in the electrode's conductivity. Nodule and aggregate sizes are inversely proportional to surface area of the material. X. Qi et al. found that as the surface area got larger and the carbon black aggregates smaller, the aggregates would block the electrode pores, leading to a decrease in electrode porosity and pore size. This then hinders the transport of electrolyte in the electrode, thus decreasing the ionic conductivity within the battery [25].

2.3.2 Layering of additives and active material

One of the controlling factors of the efficiency of the charge transport system within the electrode is the inner structure of conductive additives and how they layer with the active material.

When a conductive additive is introduced into the cathode composite, a polymer binder is often used to "glue" the additive together. This combination of conductive additive and binder creates the sub-network referred to as the electron transport system [16]. This system should under optimal layering, create many pathways for the electrons so that the whole network of overlapping branches allows for efficient electron transport.

After manufacturing the electrode, a volume of pores is created in between the conductive additive and active material (AM). The porous structure establishes a second sub-network, called the ionic transport system. However, since there are no charge carrying ions inside the electrode, the ionic transport network is not yet fully developed. When wetting the electrode with electrolyte during the cell assembly process, the pores are ideally fully occupied by the ion-conductive electrolyte [16]. This then fully establishes the ionic transport network. Again, under optimal layering, the pores filled with electrolyte should create an array of possible pathways which allows for efficient ion transport.

After a complete assembly, the structure of the wetted electrode should complete the charge transport system. In Figure 2.4 the process of establishing electron and ionic transport networks is presented. The AM in this illustration can, for example, be interchanged with LFP.
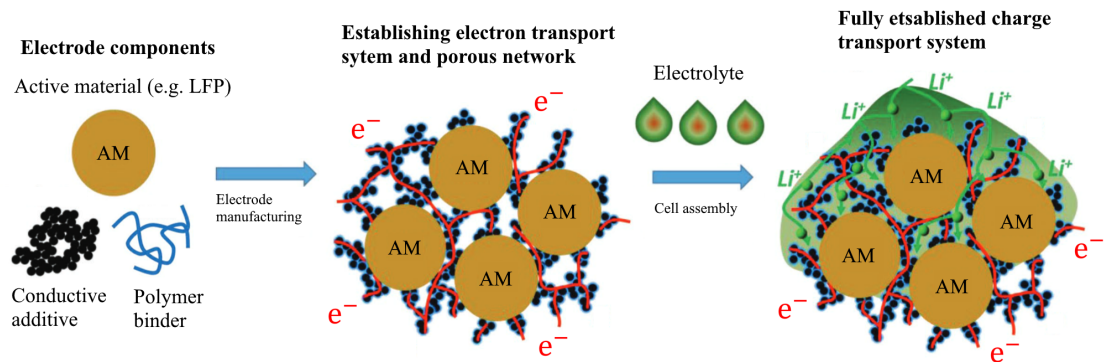
Figure 2.4: The process of establishing the charge transport system within the electrode. Figure based on illustration by Y. Wang et. al. [16]

2.4 LFP electrode slurries

A slurry is defined as a semi-liquid mixture with a suspension of solid particles [26]. The slurries used for LFP-electrodes typically contain a mixture of LFP-powder, polyvinylidine fluoride binder (PVDF), conductive carbon and n-methylpyrrolidione (NMP). The slurry is often mixed after each ingredient addition to reduce the number of agglomerates in the mixture and avoid an inhomogeneous solution that would drastically decrease the electrode efficiency [27]. PVDF is the conventional material for binding anode and cathode materials in production of Li-, Ni-, Mg- and Co-based batteries. PVDF has high chemical resistance and mechanical strength, and its insolubility and electrical properties make it a desirable binder [28]. Further, NMP is the most commonly used solvent for PVDF. It is often used in petrochemical processing, for coatings in battery manufacturing, or paint and coating removal products [29]. The BET surface area of the suspension particles largely affect the amount of NMP needed to achieve a desirable slurry viscosity. A higher surface area gives the NMP more space to seep into pores, thus requiring more NMP in the suspension. NMP has a high flashpoint ($\sim 91^\circ$C), meaning its ignition temperature makes it more stable and safe to handle than other solvents. It is also less reactive, with a lower vapour pressure, which in reducing emission of volatile organic compounds. 99% of NMP can be recycled and it is relatively chemically stable, which makes it easier to handle than other solvents. NMP is not carcinogenic, but it is considered a reproductive hazard [29], and it is therefore handled in well ventilated spaces to minimise the risks of inhalation.

2.5 Active material and thickness ratio

The active materials (AM) in an electrode are the components that react electrochemically to produce electrical energy [30]. The mass of the active material dispersed in the electrode (m_A) divided by the area it occupies (A_{elec}) is called mass loading (ML). It can be found using Equation (9), where m_{cuco} is the weight of the current collector and m_{tot} is the total weight of the electrode. Equation (8) presents the calculation of active mass. ML is often measured in mg/cm^2 for laboratory-scale batteries.

$$m_A = AM \ [\text{wt\%}] \cdot m_{tot} - m_{cuco} \tag{8}$$

$$ML = \frac{m_A}{A_{elec}} \tag{9}$$

The mass loading of the active material in an electrode has a large impact on battery cell performance. By increasing the loading, the resistance within the material decreases, which is explained by a higher number of connections. At the same time, increasing the loading level leads to longer diffusion pathways for the electrons and ions, which increases the internal resistance [31]. Therefore mass loading has to be carefully chosen for specific applications. H. Zheng et. al. found that the increase in internal resistance within the electrode observed with increasing electrode thickness, is not the main responsible factor for the significant capacity loss at higher rate for thicker electrodes, but rather that the worsening of rate capability results from Li^+-ion diffusion within the electrode. Therefore, thinner electrodes with lower mass loading typically is preferred in battery cells [32].

Another reason why thicker electrodes are not preferred, is that a large volume change between charged and discharged states result in excessive mechanical strain. This will cause mechanical disintegration of the entire electrode and rapidly degrade cycling performance [33]. There is also an increased risk of crack formation or delamination of the active mass layer from the aluminium foil in thicker electrodes [34].

2.6 Casting

Tape casting slurries are generally composed of a ceramic powder, solvent, and a number of organic components. Tape casting is used in different applications like making ceramic capacitors, electrodes in batteries and thin films. The aim of casting is to make a uniform and dense cast with good shear thinning behaviour and high solid loading. Heat treatment and drying steps are done to evaporate the solvent from the surface. This can be sped up by applying air drying, but evaporation should be controlled to make sure that the cast does not crack or curl [35]. Calendering is sometimes used at the end to lower their porosity, give them uniform thickness and an even structure within the electrode surface [27]. This is performed by compressing the cast with a roller which is set to a predetermined thickness based on the initial thickness of the cast.

2.7 Assembly conditions

Research on LIBs is often conducted on half-cell configurations to evaluate electrodes separately. Lithium metal is typically used as both counter and reference electrode when the focus of analysis is the cathode. This differentiates from full-cells, where a graphite anode is often utilised [36].

A glovebox is a sealed container with a strictly controlled environment that is usually employed for laboratory battery assembly. Rubber gloves are placed in the transparent wall of the container, making it possible to handle the objects inside the box. A glovebox used for battery-making or battery research is usually filled with argon gas, because of lithium's high reactivity with air and water, and because the electrolyte can easily degrade in contact with atmospheric

conditions. It is desirable to keep the levels of oxygen and water between 0.1-1.0 ppm [37]. For objects to be inserted into the glovebox, they first have to be placed inside an antechamber connected to the glovebox. The air has to be evacuated several times to remove all traces of air and moisture [38].

2.7.1 Types of cells

For researching battery properties, commercial machine-made batteries provide very reproducible data [39]. This would make them ideal for comparative analysis. However, machine-made cells are made in large batches and require pre-made production structures and a significant amount of resources. It would then be impractical to produce a whole batch of commercial cells to investigate an array of different battery components [39] [40]. This is why, for example, academic evaluation of material properties in batteries are done on hand-made cells. The three most common cell configurations in laboratory-scale research are pouch cells, coin cells and Swagelok cells [41].

2.7.2 Coin cells

Coin cells are utilised because of their relatively easy assembly and low cost [40]. There are many types of coin cells, and the International Electrochemical Commission (IEC) standard 60086-3 was established to differentiate them. Not every manufacturer uses the IEC standard and conventions may vary, but an example battery cell conforming to the IEC standard is "CR2032". The first letter in the name is the code which indicates the primary material used, and in this case "C" is lithium. The second letter indicates the shape of the cell, "R" for a round form. The remaining numbers indicate the size parameters of the cell. In the example, "20" denotes a 20 mm cell diameter and "32", a cell height of 3.2 mm [42]. The composition of a coin cell may vary slightly, but a general schematic representation of a typical coin cell can be seen in Figure 2.5.
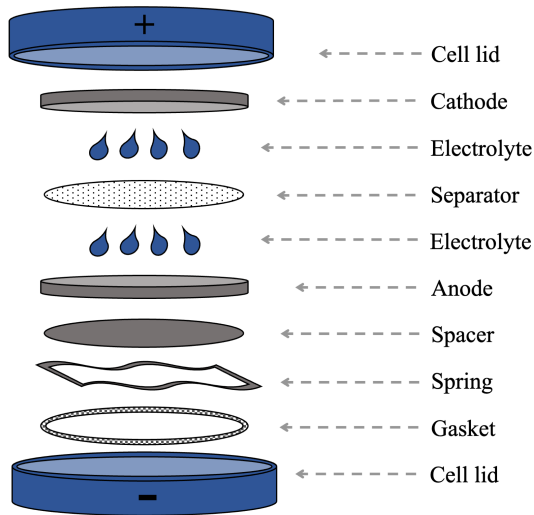
Figure 2.5: The components of a half-cell.

The cell lids, springs and spacers within a coin cell are most commonly made from stainless steel [41]. A spring is used to ensure a uniformly compact cell after the cell is crimped. The spacer serves as a filler-material and as a way to uniformly spread the compacting forces from the spring. The spacer can vary from 0.2 mm to 1 mm in thickness. In most cases the separator is a thin sheet of microporous polymer [41]. Its purpose is to physically isolate the cathode and anode. This does not only prevent short circuiting, but also facilitates effective transport of ionic charge carriers within the electrochemical cell [43]. The electrodes are cut into discs with a diameter usually ranging between 12 to 18 mm. The electrolyte consists of soluble salts in a liquid matrix and serves as the conductive catalyst by enabling ionic transport between the electrodes during charge and discharge. In LIBs, for example, the liquid electrolyte is a solution of lithium salts with organic solvents [44]. The electrolyte volume is typically controlled between 10 and 100 µL depending on the cell. [41].

2.8 Characterisation methods

2.8.1 BET

The BET theory was presented in 1938 by the chemists and theoretical physicists Stephen Braunauer, Paul Hugh Emmet and Edward Teller. The theory is an extension of a model developed by chemist and physicist Irving Langmuir in 1916, which correlates the adsorption of a singular layer of gas molecules on a solid surface to the gas pressure above the solid surface. Nitrogen gas is commonly used because of its availability and strong adsorption interaction with most solids. To strengthen the interaction between the gaseous and solid phases, liquid nitrogen is used to cool down the surface and keep the temperature stable [45]. Braunauer, Emmet and Teller extended Langmuir's model to contain an infinite number of layers, shown in Figure 2.6. BET surface area is measured in m^2/g.
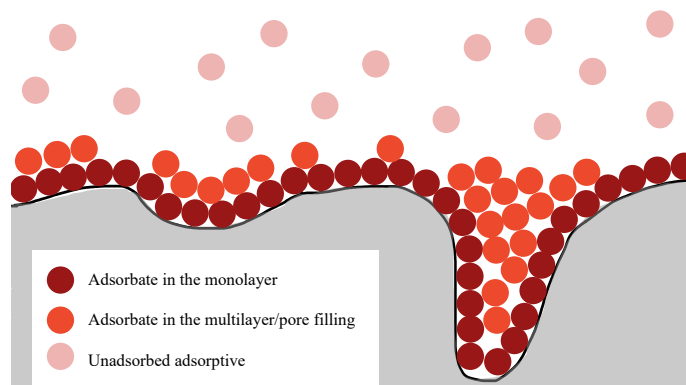
Figure 2.6: Illustration of the principle of BET theory. The gas molecules form layers around the particle. Illustration inspired by Anton Paar [46].

2.8.2 XRD

X-ray diffraction is a method of analysis used in many different fields of study. The technique can be used to acquire information such as the crystal structure of materials, the presence of impurities and the phase purity. The analysis is executed by using a diffractometer, which is made up of three main parts: a radiation source, sample holder and detector, as shown in Figure 2.7. The wavelength of the emitted X-rays varies depending on the X-ray source material. Copper and cobalt are common materials for this application.
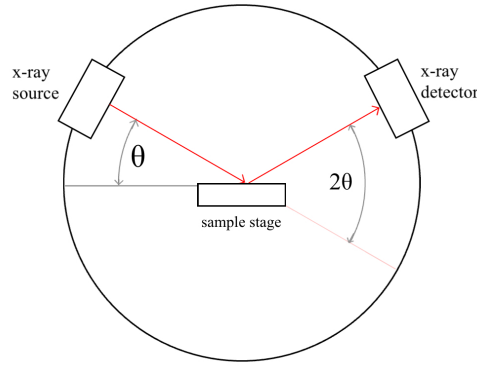
Figure 2.7: Simple illustration of a diffractometer's most important components. Inspired by xrd.co [47].

In regular powder XRD, the X-rays are focused towards the sample at a continuously varying angle. The X-rays diffract off the sample depending on the input angle and the crystal structure of the sample. Constructive or destructive interference determines the appearance of the resulting XRD pattern. Figure 2.8 shows the diffraction process in a material through two crystal planes separated by the distance d_{hkl}.
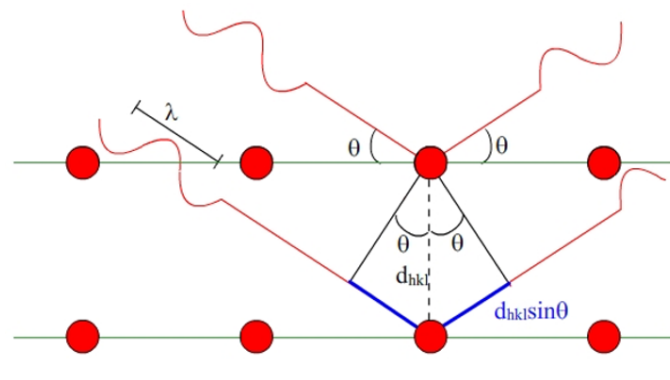
Figure 2.8: Illustration of the XRD mechanism. X-rays hit the different crystal planes, causing interference that reflects back to the X-ray detector at angle θ [48].

The rays will only be detected when constructive interference occurs. Bragg's law states the correlation between wavelength (λ), angle (θ) and distance between crystal planes by Equation (10).

$$2 \cdot d_{hkl} \cdot \sin(\theta) = n \cdot \lambda \tag{10}$$

Intensity of the diffraction is measured and plotted against 2θ, creating a diffractogram that is unique to the material in question. The diffractogram is usually compared to either calculated diffractograms or past measurements given in a public database to identify the material's characteristics.

2.9 Battery testing

2.9.1 Rate performance testing

The most common way to map the performance of a LIB is by charge/discharge cycling. Charging an electrode and then discharging it is referred to as a cycle, and only one (dis)charge is called a half-cycle. Charging and discharging a battery with a constant current (CC) is called galvanostatic cycling, and cycling using constant voltage (CV) is called potensiostatic cycling. Further, C-rate is a term used when discussing galvanostatic charging, and gives a value of the current needed to charge a battery to 100% state of charge (SoC) after n hours. It is defined as the expected capacity (C) of the electrode divided by the number of hours (n) to fully charge or discharge that capacity [41], as shown in Equation (11).

$$\text{C-rate} = \frac{\text{C}}{n} \tag{11}$$

For instance, when a battery is charged at a 1C rate, it reaches full charge within one hour, whereas a 2C charging rate achieves full charge in just 30 minutes.

2.9.2 Cycling methods

There is an array of different metrics that can be obtained from cycling. Therefore, different cycling methods or protocols have been established. Some of the most used are: Galvanostatic Cycling with Potential Limitation (GCPL), Potentiodynamic Cycling with Galvanostatic Acceleration (PCGA) and Constant Current Constant Voltage (CCCV). GCPL is the standard protocol for studying the general behaviour of the cycled cells. A cell's performance is measured as a function of its charge and discharge behaviour. It is mostly measured as the number of hours needed for the nominal battery capacity to pass through. When using GCPL, it is possible to monitor the potentials of both the positive and negative electrodes against a reference, which is usually lithium metal. This makes it possible to independently follow the cycling behaviour of each electrode material [49]. In PCGA, the electrode is cycled under a stepwise potentiodynamic program. A potential sweep is done with a set amplitude and duration. This protocol can be used to measure the chemical diffusion flux of the sample as a function of time. The sample is provided constant current during the swipe [50]. LIBs are usually charged using a constant current constant voltage (CCCV or CC/CV) charging profile, where the cell is charged using a constant current until its voltage reaches the specified voltage limit. This is usually when the cell is between 70% and 80% SoC. The cell voltage is then kept constant to ensure a smooth charging of the last 20-30%, resulting in an exponential decrease of the charging current. A current limit is often set to avoid damaging the cell. The current limit is often set to 3-5% of C-rate in academia [51]. When testing a cell with CCCV, a formation step is used to grow a high quality

SEI layer on the anodes to minimise cell failure probability and maximise cell performance. This formation step takes place at very low C-rates, typically C/20 or C/10 [52].

During a CCCV protocol, it is possible to do a rate capacity test or a rate performance test. The former test is based on charging and discharging a battery cell at a constant C-rate to determine its potential cycle life. The latter checks the performance of a cell at different C-rates to see how fast the cell can be charged/discharged and how it affects the CR.

Figure 2.9 presents a hypothetical CCCV charging curve for commercial LFP at 1C, with the cell voltage and current through time. The cut-off voltages are arbitrarily set to 3.65 V and 2.00 V. The graph includes a visualisation of the CC to CV transition step, where the SoC is 70-80%. To ensure that the SoC is 100% when discharging, the voltage is held constant for some time with exponentially decreasing current. This is because while the battery has reached the voltage limit, Li^+-ions are still being transferred throughout the battery [51]. Figure 2.10 pictures a theoretical discharge curve for commercial LFP where the current is constant.
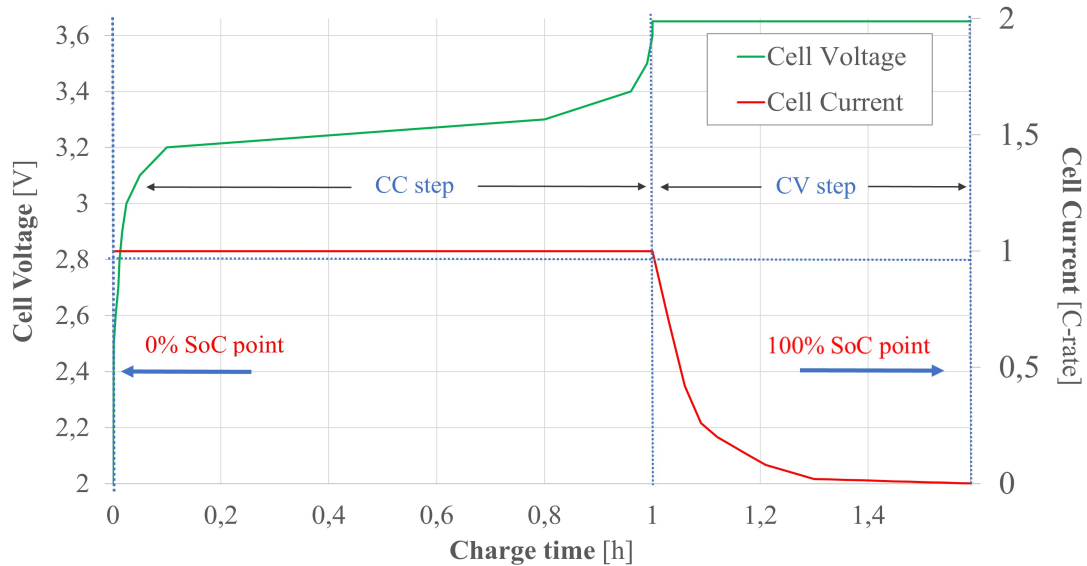
Figure 2.9: Typical behaviour in a CCCV-charging-curve for LFP at 1C. Graph inspired by Ed Brorein's visualisation of a standard charge-discharge protocol for LIBs [51]. Values are indicative.
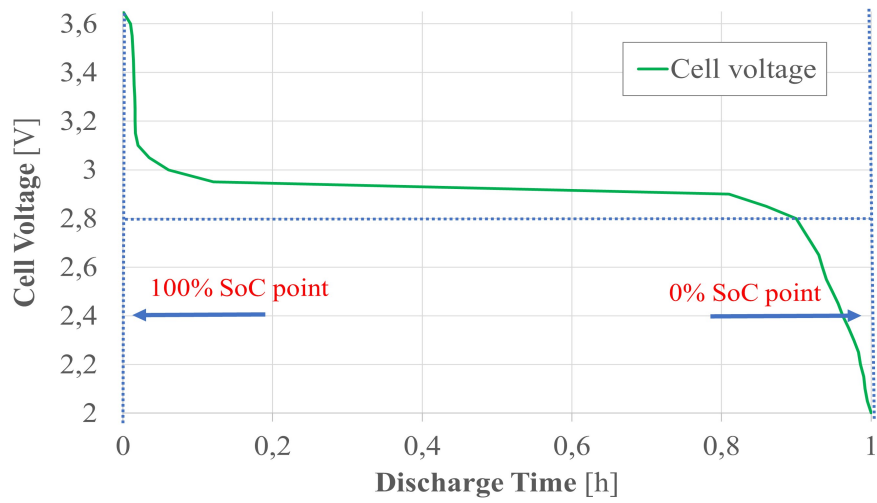
Figure 2.10: Typical behaviour for a discharge cycle for LFP at 1C. Graph inspired by Ed Brorein's visualisation of a standard discharge curve [51]. Values are indicative.

3 Experimental

To achieve the aim of the project, a step wise experimental method was executed. A representation of the experimental work is provided in the following flowchart in Figure 3.1. Risk assessments done prior to experimental work is presented in Appendix A.
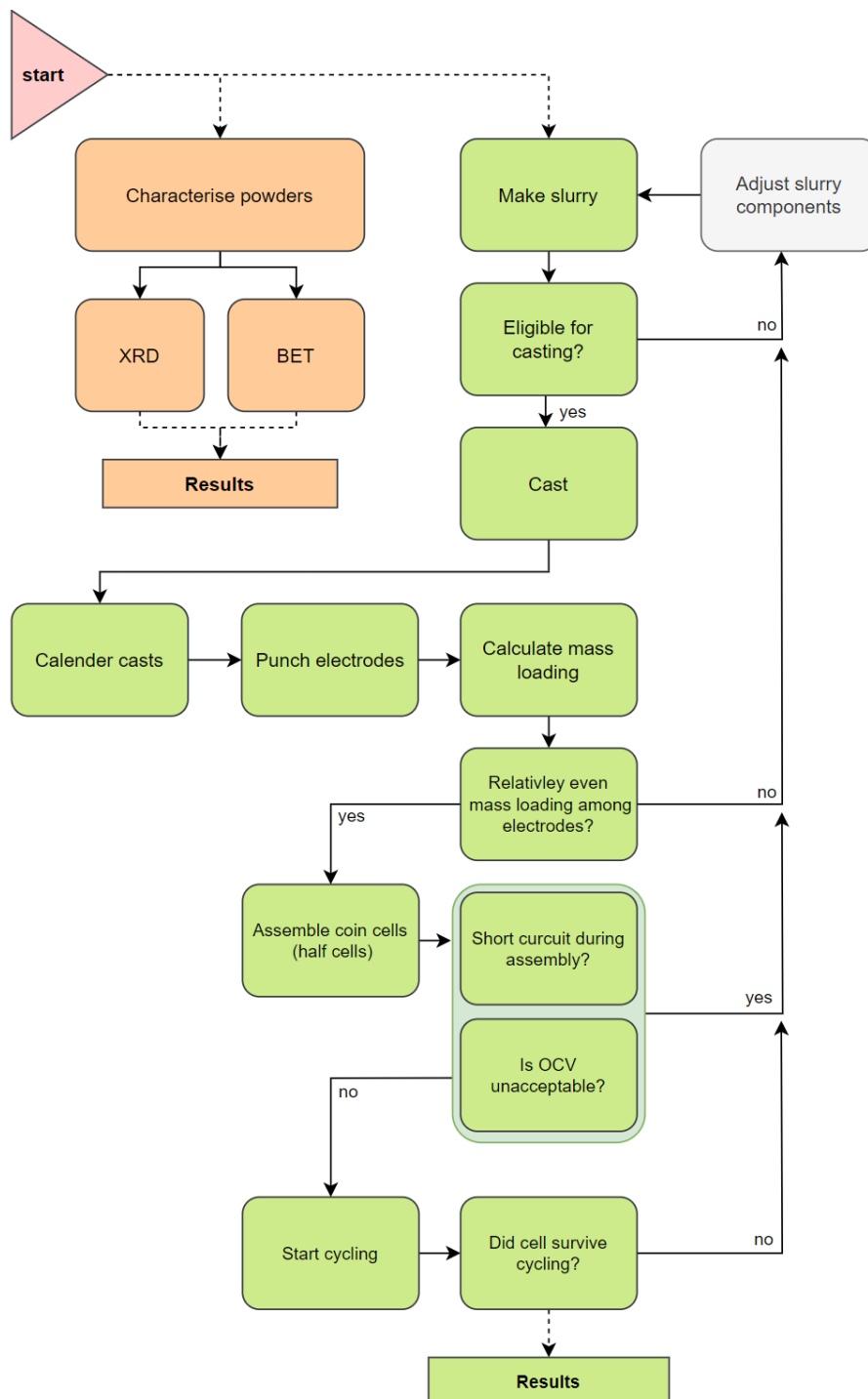
Figure 3.1: Flowchart visualising the experimental work.

3.1 Powder Characterisation

In this report, three unique conductive carbon blacks were investigated: i.e, SUPER C45, Ketjenblack and SFG15L. A description of the carbon samples is presented in Table 3.1.

Table 3.1: Description of each of the three samples with their full name, abbreviation, colour and visual powder characteristics.

Full name	Abbreviation	Colour	Powder characterisation
SUPER C45	C45	Black	Fine
Ketjenblack	KB	Dark black	Very fine
SFG15L	SFG	Grey black	Flakey

3.1.1 BET

The three conductive carbon blacks and LFP powder were examined with the use of BET analysis. First, an appropriate mass estimate needed for the analysis was found for each sample. The mass was calculated from approximate data sheet values of the BET surface area. The calculations are shown in Equation (12), and the resulting values are given in Table 3.2. The appropriate surface area (column 4 in Table 3.2) was an approximate value given by the lab-manager based on previous experience with BET.

$$\text{Appropriate weight} = \frac{\text{Appropriate surface area}}{\text{BET surface area estimate}} \tag{12}$$

Table 3.2: Appropriate sample weight for BET analysis.
Calculations done through Equation (12), with BET surface area estimates and appropriate area as parameters.

Sample	BET surface area estimate [m^2/g]		Appropriate surface area [m^2]	Appropriate sample weight [g]
	Range	Average		
C45	44-46	45		0.44
KB	900-1300	1100	20	0.02
SFG	8-10	9		2.22
LFP	10-14	12		1.67

These values were necessary to establish to control the time duration of the gas adsorption analysis. An analysis of a sample with a large BET surface area takes longer. It was therefore important to have an appropriate sample amount, so that a desired analysis duration could be achieved.

The appropriate masses were weighed out and each sample was placed in its own test tube. The test tubes were placed in The Micromeritics SmartPrep Degasser for degassing. After degassing, the respective test tubes were inserted into the Micromeritics TriStar 3000 V6.08 gas adsorption analyser.

3.1.2 XRD

To examine the crystal structure of the LFP and conductive carbon powders, X-ray diffraction was used. To prepare sample for analysis, the powders were carefully transferred to their own sample holder in a fume hood. A glass slide was used to horizontally align the powders to create an even surface with the sample holder. Individual Kapton film strips were used to cover the samples. The XRD measurement parameters were then set. The 2θ-range was set to 0-75°. The divergence slit opening was set automatically at V6, a constant 6 mm opening. The four samples were then inserted into the Bruker D8 A25 DaVinci X-ray Diffractometer, with a LynxEye SuperSpeed Detector, by laboratory personnel.

3.2 Cathode preparation

3.2.1 Slurry

The slurries used for all the cathodes, was mixed with a combination of carbon coated LFP powder (Life Power P2 Clariant), conductive carbon black (CB), PVDF binder and NMP.

An abbreviated notation is used to simplify the cathode compositions in wt%. As an example: $8:1:1$, indicates that the cathode materials consists of 80 wt% X, 10 wt% Y and 10 wt% Z. Solid content (SC) is referred to as the accumulated percentage of all the dry components, LFP, CB and PVDF (powder part of binder) utilized in each slurry.

The active material slurry contained a ratio of $93:3.5:3.5$ LFP : CB : Binder. The binder consisted of PVDF dissolved in NMP with a ratio of $2:23$, mixed using a magnetic stirrer for two days. A mixture with SC of 51% was tested. The weight of all components were based of the amount of LFP used in the mixture. Calculations of the different weight distributions can be seen in Equation (13a - 13d). Here $PVDF_B$ and NMP_B referrers to the PVDF and NMP used specifically in the binder.

$$CB\;[g] = \frac{LFP\;[g]}{LFP\;[wt\%]} \cdot CB\;[wt\%] \tag{13a}$$

$$Binder\;[g] = \frac{LFP\;[g] \cdot PVDF_B\;[wt\%]}{LFP\;[wt\%] \cdot PVDF\;[wt\%]} \tag{13b}$$

$$\text{Slurry [g]} = \left(\frac{\text{LFP [g] + CB [g] + Binder [g]}}{\text{PVDF [wt\%]} \cdot 100} \right) \cdot 100 \tag{13c}$$

$$\text{NMP [g]} = (\text{Slurry [g]} \cdot \text{NMP [wt\%]}) - (\text{Binder [g]} \cdot \text{NMP}_\text{B} \text{ [wt\%]}) \tag{13d}$$

The conductive carbon powder was weighed and added to a mixing container. Binder was then pipetted into the container. After this, the solution was mixed in a TMAX-TP300S Vacuum Planetary Centrifugal Mixer at 2000 rpm for 5 minutes. After mixing, LFP was added, as well as half of the needed NMP. This was mixed once again at 2000 rpm for 5 minutes. The rest of the NMP was added in five batches, and mixed between each batch.

A SC of 51% was made for C45 and SFG, but this did not work for KB and the SC was then reduced to 30%. The SC of C45 and SFG was lowered to 40% to match the SC of KB, to retain their comparability while avoiding excessively low viscosity. The SC of the conductive carbon slurries is presented in Table 3.3.

Table 3.3: Percentage distribution of SC to NMP for each of the slurries.

Conductive carbon	Solid content	NMP
C45	40%	60%
KB	30%	70%
SFG	40%	60%

3.2.2 Casting

The finished slurry was cast on a 0.02 mm thick 1060-H18 aluminium sheet with a height of 200 µm using a RK K Control Coater tape caster. The casts were placed inside a heating oven at a temperature of 60-80°C overnight for drying.

3.2.3 Calendering

After drying, the casts were removed from the heating oven and cut to appropriate size to make them easier to handle, measure and calender. The thickness of the casts was measured on multiple points and an average for each cast was calculated. The casts were calendered once at 85% of the casts' average thickness to obtain a more compact electrode.

3.2.4 Punching and mass loading

After calendering, electrodes were punched out from the cast using a Gelon manual electrode puncher to a size of 12 mm diameter. The average mass loading of active material was then calculated, based on the weight of the electrode divided by the area of the electrode, shown in Equation (9).

3.3 Coin cell preperation

3.3.1 Assembly

Celgard 2400 separators with a radius of 18 mm, were punched out using a handheld hollow hole puncher and a small hammer. The coin cell assembly was conducted in an MBRAUN labmaster pro glove box filled with dry argon gas. The electrodes were dried at 120°C in vacuum overnight, before they were transported into the glovebox.

The gasket was placed inside the anode lid of the coin cell. Then, the wave spring and the spacer, with a thickness of 1 mm, were positioned inside the gasket. A lithium chip was brushed to remove the oxide layer from the surface, then placed on top of the spacer, working as the anode of the cell. 25 μL LiPF$_6$ EC/DEC 1:1 electrolyte was pipetted on top of the Li chip, and a separator was placed over it, before another 25 μL were pipetted onto the separator. The cathode was placed on the separator, and the top lid was aligned on top of it all. The order of components is shown in Figure 3.2.
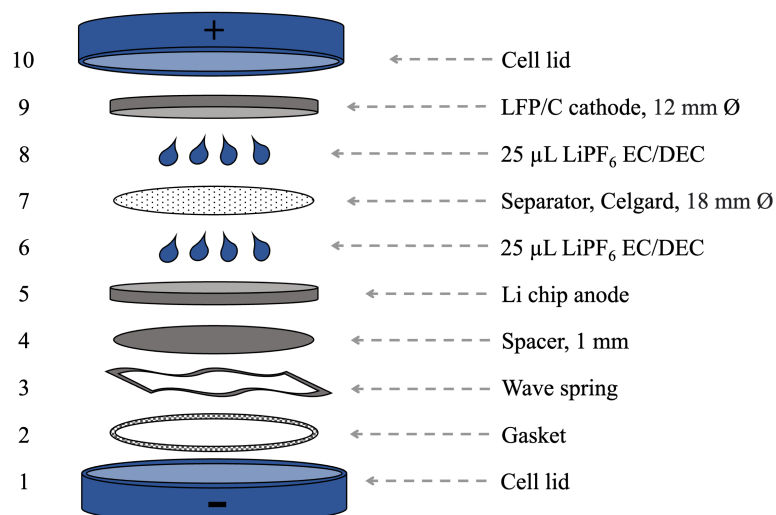
Figure 3.2: The order of components of half-cell assembly.

The coin cells were then crimped using a Hohsen Automatic Coin Cell Crimper, and the open circuit voltage was measured with a multimeter. The batteries were placed in separate zip-lock bags and removed from the glovebox. Two fully assembled cells is shown in Figure 3.3.

Figure 3.3: Fully assembled coin cells.

3.4 Galvanostatic cycling

The performance of the fully assembled half-cells were tested through galvanostatic cycling. The coin cells were attached, with electrical connections, to the Biologic BCS-805 battery cycler, and tested using a rate capability program. The program consisted of three charges and discharges at the following C-rates: C/10, C/3, C/2, 1C, 2C, 5C, and C/3. An illustration of the steps is shown in Figure 3.4. The steps were calculated using Equation (11). The average active mass was calculated using Equation (8) and is provided for each carbon cathode sample in Table 3.4.
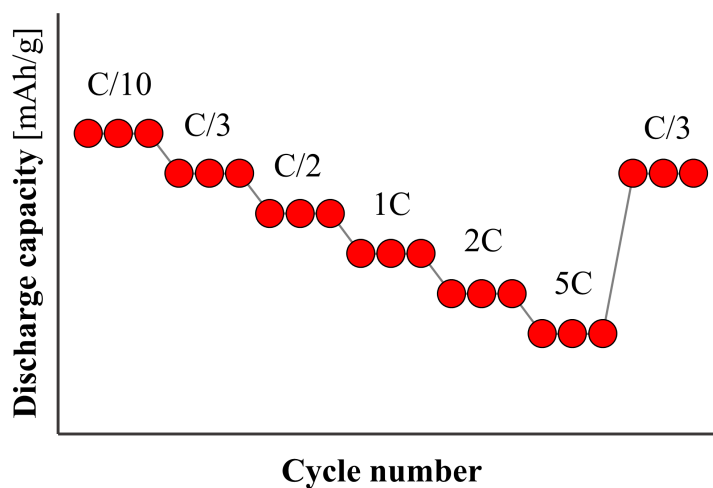
Figure 3.4: Illustration of the steps of the half-cell cycling program.

Table 3.4: Average active mass for the three samples.

Sample	Active mass [mg]
C45	7.15
KB	5.11
SFG	7.42

The required current for each C-rate for C45, KB and SFG was calculated based on the theoretical capacity of LFP through Equation (5), and is given for 1C in Table 3.5 with a 30% current limit for the C-rate of each carbon sample. Further calculation for each of the C-rate steps is shown in Appendix B (Table B.1, B.2 and B.3).

Table 3.5: 1C for samples C45, KB and SFG with a 30% current limit

Sample	1C [mAh]	Current limit [mAh]
C45	1.215	0.365
KB	0.868	0.260
SFG	1.261	0.378

4 Results

4.1 Powder characterisation

4.1.1 BET

The respective BET surface area of the three conductive carbon blacks and LFP are presented Table 4.1. The experimental data match the BET values found in the commercial data sheets for the powder samples. The surface area of C45 and KB is roughly 3.5, and 100 times larger than that of the LFP particles. Meanwhile, the surface area of SFG is 0.7 times smaller than the LFP particles.

Table 4.1: BET surface area of the conductive carbons and LFP. The relation between the conductive carbons and the active material is given.

Sample	BET surface area $[\mathrm{m}^2/\mathrm{g}]$	Relation to active material [-]
C45	46.5	3.5
KB	1331.97	101.1
SFG	9.45	0.7
LFP	13.17	1

4.1.2 XRD

Figure 4.1 shows the diffractograms of the conductive carbon blacks and LFP. Each sample is coloured to differentiate them. The vertical lines in black and red are theoretical diffractograms generated through the program VESTA [12] with data from the Crystallography Open Database (COD). Pure carbon graphite diffractogram was used for comparison with the carbon blacks. The COD IDs are:

- C (graphite): 1000065 [53]
- LiFePO$_4$: 7244316 [54]

From the diffractograms it can be seen that C45 and KB have an amorphous structure. The peaks are poorly defined, and exhibit a large deviation between the intensity counts. The peaks of KB are discernibly wider than those of C45. KB can then be considered more amorphous than C45. SFG, on the other hand, exhibits a sharp peak at a 2θ value of $\sim26°$, accompanied by some smaller, less defined peaks. The peaks coincides with those of the theoretical graphite. SFG was then characterised as a highly crystalline carbon, similar to graphite. The last diffractogram shows that the LFP sample tested is comparable to the composition and structure of pure LiFePO$_4$. The theoretical generated peaks from COD match the experimental peaks to a great extent, with no unidentified peaks, giving an indication of high phase purity of the LFP.
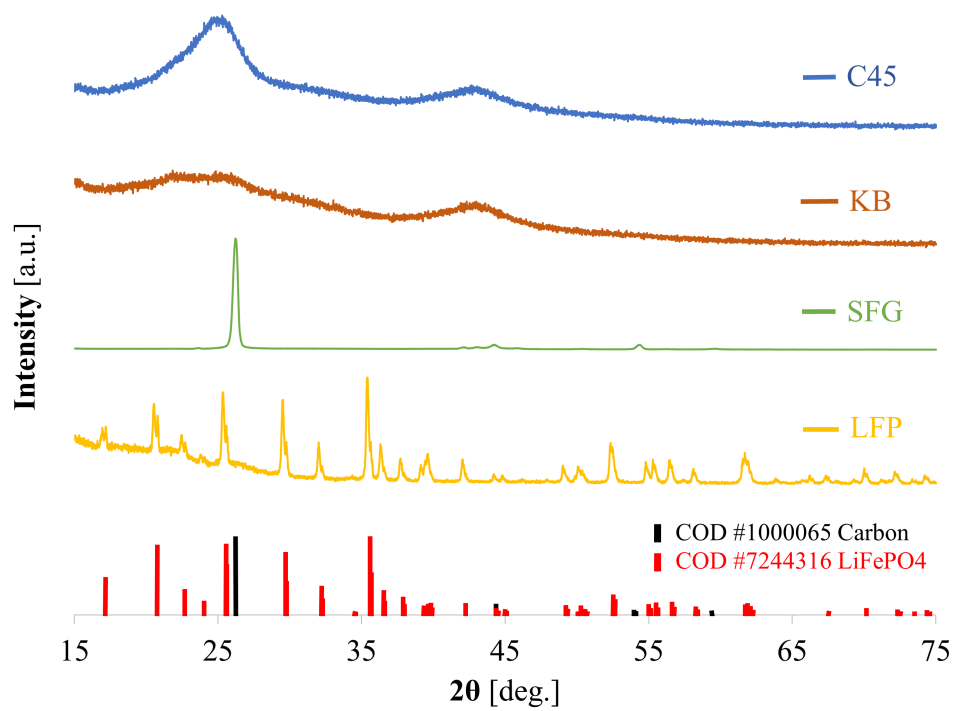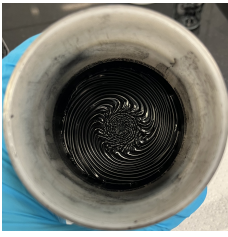
Figure 4.1: Diffractogram of the conductive carbons and the active material. COD IDs graphite from D. E. Nixon et. al. [53] and LFP from S. F. Mayer et. al. [54].

4.2 Slurry and casting

Table 4.2 presents the tested and used solid content (SC) for each cathode composition containing the conductive carbons C45, KB and SFG. A depiction of each slurry and resulting cast is shown. Note that no picture of the tested C45 and SFG slurry was taken. They resembled in large part the used slurries in viscosity. The C45 cathode composition with 51% and 40% SC gave slurries with a low viscosity and resulted in casts with a smooth and matte surface. The KB cathode composition with 40% SC resembled mud in texture and was very viscous. The resulting cast cracked up and was unusable. When lowered down to a SC of 30%, the slurry was less viscous and the cast was usable. The cathode composition with SFG resembled in large part C45 at both 51% and 40% SC. The slurries had a low viscosity and the casts were smooth. Even at 30% SC the mixtures containing KB were more viscous than C45 and SFG. The SC was not lowered further due to health concerns relating to NMP.

Table 4.2: The tested and used solid contents of each type of cathode composition. Each resulting slurry and cast is depicted.

Sample	Solid content [%]		Slurry		Cast	
	Tested	Used	Tested	Used	Tested	Used
C45	51	40	-			
KB	40	30				
SFG	51	40	-			

The average mass loading of each cathode type after punching is presented in Figure 4.2. The values shown are averages of three cathode discs and their standard deviation is presented. C45 and SFG achieved mass loadings of $\sim$6.4 mg/cm^2 while KB obtained a mass loading $\sim$30% lower, with an average of 4.5 mg/cm^2. A relation between the lowered SC and the resulting lower mass loading of KB can be observed.
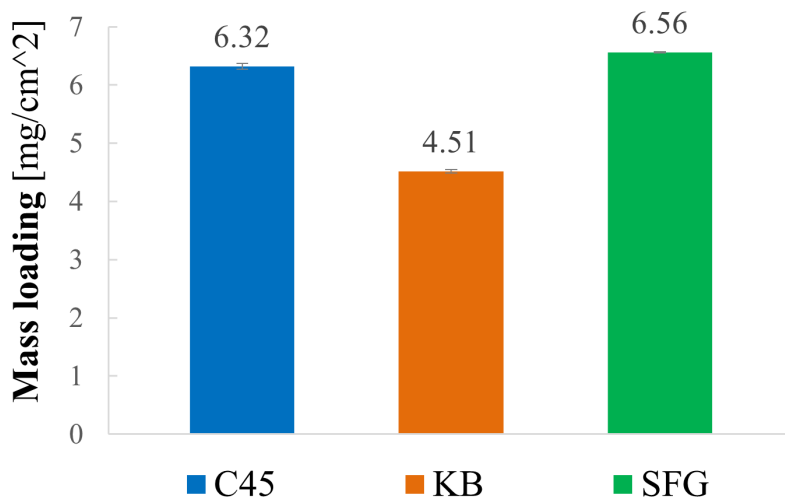
Figure 4.2: Average mass loading of the cathodes containing the three conductive carbons. C45 and SFG have similar mass loadings, while KB is notably lower.

4.3 Individual battery cycling results

The following graphs show the cycling results of the three different samples of half-cells. Each containing LFP cathodes with the three conductive carbon black samples. All replicate results can be seen in Appendix C. Three replications of each half-cell sample were put through a cycling protocol. When presenting the cycling numbers (N), the count of cycles start at 0, thus N = 0 gives the first cycle of the formation step of C/10.

4.3.1 C45

The open circuit voltages (OCV) of the three half-cells with C45 containing cathodes are shown in Table 4.3. Two of the C45 cells do not reach the average potential of LFP at 3.4 V [1]. In Figure 4.3, the voltage profile over the total cycling time of the C45 cells is presented. The three C45 cells are coloured to differentiate them. A discerning difference was observed between the parallels. $C45_1$ and $C45_2$ behaved according to the pre-set CCCV protocol, but $C45_3$'s low OCV contributed to a shorter cycling time.

Table 4.3: OCV of the C45 cells.

Sample	OCV [V]
$C45_1$	2.91
$C45_2$	3.40
$C45_3$	1.25
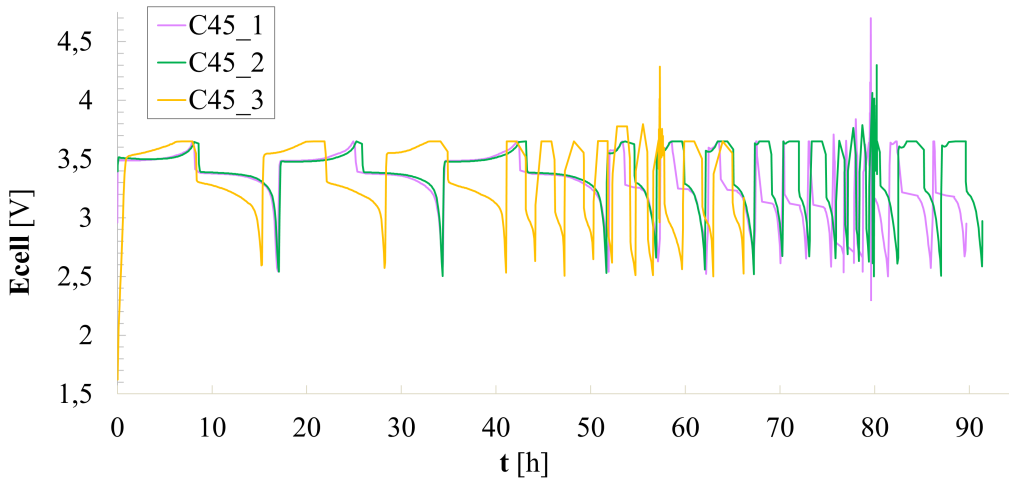
Figure 4.3: The full cycling program for the three C45 cells, with an applied voltage window between 2.50 and 3.65 V.

The discharge capacities for the first formation cycle are presented in Table 4.4, and Figure 4.4 provides a graphic representation. A satisfactory output compared to the theoretical capacity of LFP was achieved, with the cells reaching 84.8% of the capacity on average.

Table 4.4: Specific discharge capacities for the first formation cycle at (C/10) for the C45 cells.

Sample	Discharge capacity [mAh/g]
C45$_1$	144.8
C45$_2$	144.9
C45$_3$	143.0
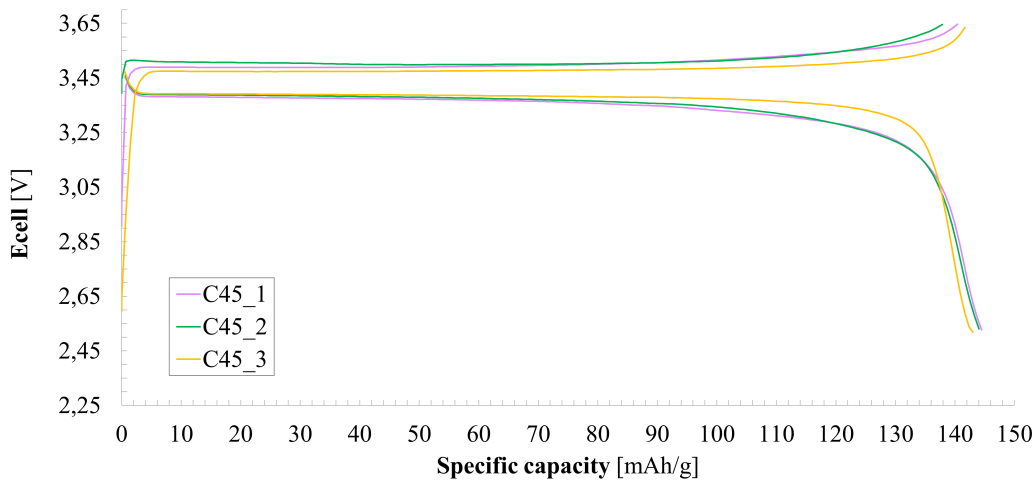
Figure 4.4: The charge/discharge curves of the first formation cycle at C/10 for C45 cells. The specific discharge capacities are obtained from the x-axis intersection at the end of the lower discharge curve.

The discharge capacities for each cycling step are presented in Figure 4.5. Each data point is the average value of the three parallels of C45 cathodes, given with their standard deviation. The cells drop to a capacity of 125, 100 and 70 mAh/g for C-rates C/3, C/2 and 1C respectively. During the high rate of 2C, the capacity drops drastically, averaging 10 before the capacity drops to 0 at 5C. At capacity retention test step the cells averaged 105 mAh/g. As seen in Figure 4.6, the CE of all rates except 2C and 5C are sufficiently high, even at the last capacity retention step at C/3, with values above 95% CE. During 1C a decrease down to 90% CE can be observed. The capacity retention for C45 is presented in Table 4.10.

Figure 4.5: The average rate performance of the C45 cells. Standard deviations were derived from three cell replications.

Figure 4.6: The average Coulombic efficiency plotted for each cycle for the C45 cells. CE at 2C and 5C were set to 0% due to cell failure at these rates. The standard deviation was derived from three cell replications.

4.3.2 KB

The KB cells gave OCV readings near 3.4 V, as shown in Table 4.5. The highest difference among the three cells was 0.02 V. The cycling profile of the KB cells is presented in Figure 4.7, where each KB cell's profile operated as intended. After roughly 80 hours voltages exceeding the set cut-off of 3.65 V can be seen. As seen in red, KB_2 finished roughly 6 hours before the two other cells.

Table 4.5: OCV of the KB cells.

Sample	OCV [V]
KB_1	3.36
KB_2	3.35
KB_3	3.37
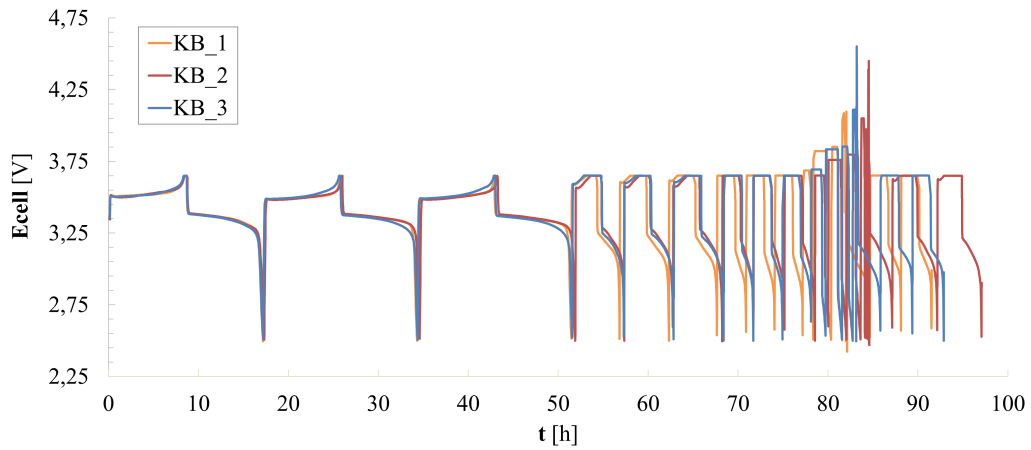
Figure 4.7: The full cycling program of the three KB cells. Cut-off voltages were 2.50 and 3.65 V.

Table 4.6 presents the discharge capacities for the first cycle at C/10 for the three KB cells. Capacities near LFP's theoretical capacity was obtained, with 85.5% of the value. A graphic representation of both the charge and discharge curves are presented in Figure 4.8, where cell potential is plotted against specific capacity.

Table 4.6: The specific discharge capacity values reached at the first cycle at C/10 for the three KB cells.

Sample	Discharge capacity [mAh/g]
KB_1	146.2
KB_2	144.9
KB_3	145.0

Figure 4.8: The charge and discharge curves of the first cycle at C/10 of the three KB cells. The specific discharge capacities can be read at the end of the lower discharge curve.

Average rate performance values for the KB cells are presented in Figure 4.9. The discharge capacities reached at C/10 are given in Table 4.6. The cells reach 140, 105 and 70 mAh/g in the C-rates of C/3, C/2 and 1C. In the heavier loadings of 2C and 5C, the cells reach 5 and 0 mAh/g, respectively. The returning C/3 steps average ∼110 mAh/g in capacity, but experience a large drop after the first cycle.

Figure 4.10 shows the CE of the KB cells. Because the cells failed at 2C and 5C, these CE values were set to 0%. At all rates except 1C, the cells average a CE of ∼97%. During 1C the cells average 70% CE with a significant drop in the second cycle. The capacity retention through the two C/3 steps is presented in Table 4.10.
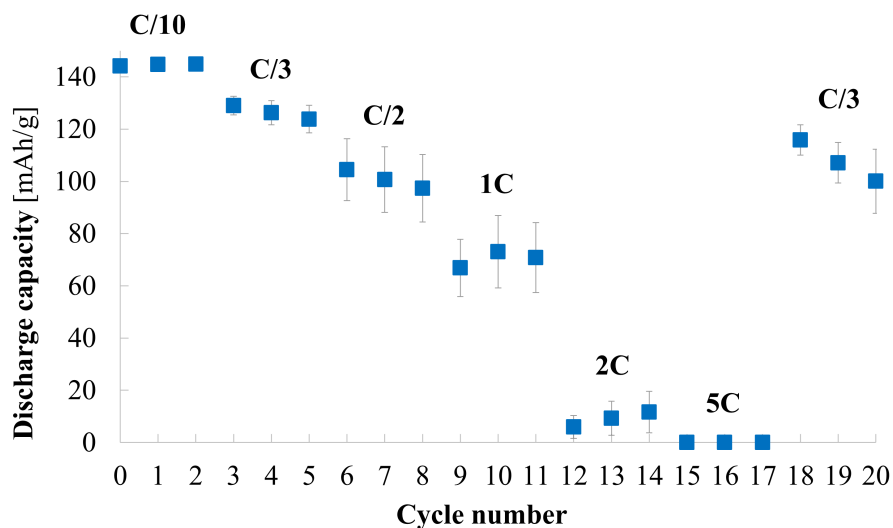

Figure 4.9: The average rate performances for the KB cells. Standard deviations were derived from three cell replications.
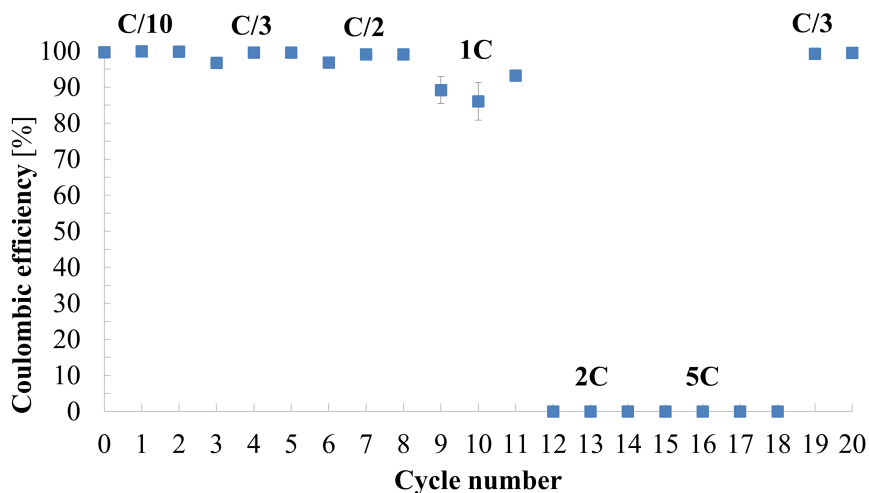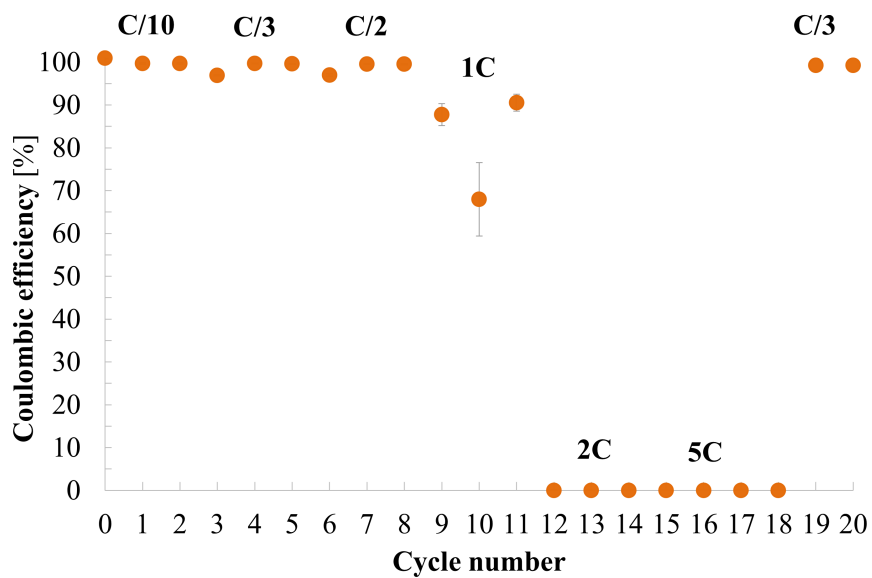
Figure 4.10: The average Coulombic efficiency plotted for the three KB cells. CE at 2C and 5C were set to 0% due to cell failure at these rates. The standard deviation was derived from a parallel of three replicates.

4.3.3 SFG

The OCV of the SFG cells are presented in Table 4.7. The values are close to the average OCV of LFP at 3.4 V, only maximally deviating by 0.06 V. The cycling profile, however, is not satisfactory, with a staggering observed for all three SFG profiles. The cells all finish their cycling at significantly different times, with SFG_1 running 50% longer than the other two cells.

Table 4.7: OCV of the SFG cells.

| Sample	OCV [V]
SFG_1	3.34
SFG_2	3.39
SFG_3	3.38
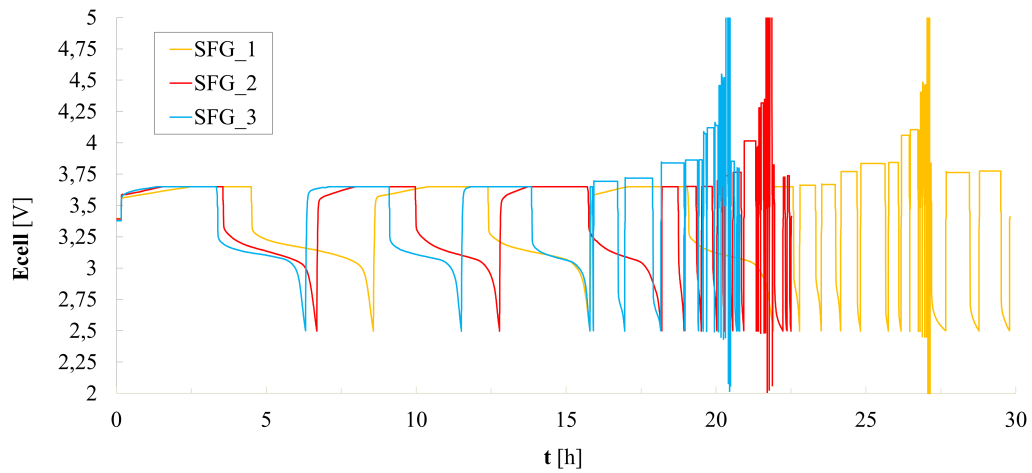
Figure 4.11: The full cycling program of the three SFG cells. Cut-off voltages were 2.50 and 3.65 V.

The cells' discharge capacities at the first formation cycle of C/10 are presented in Table 4.8. The average capacities reached only 28.5% of the theoretical capacity of LFP. The charge/discharge curve for the first cycle at C/10 is plotted in Figure 4.12.

Table 4.8: The specific discharge capacity values reached at the first cycle at C/10 for the three SFG cells.

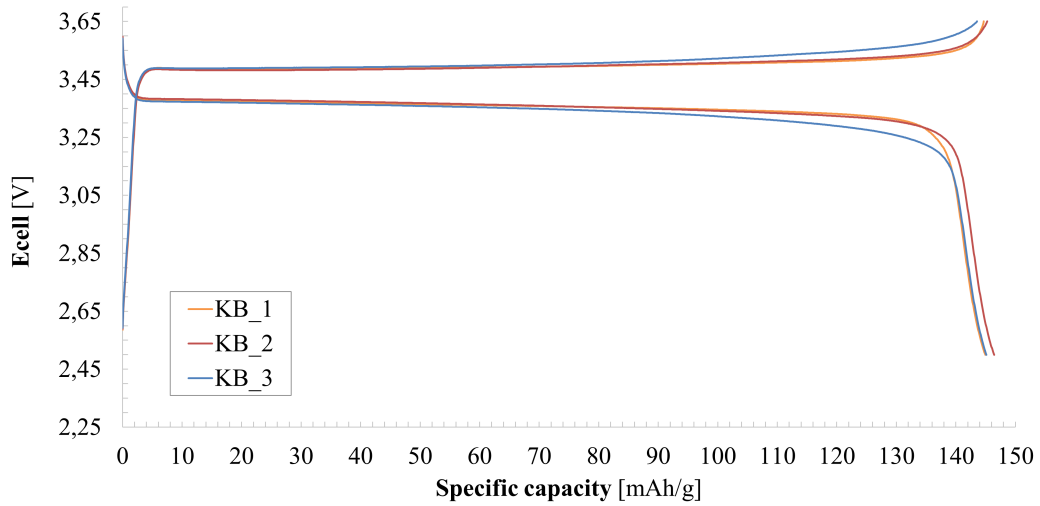| Sample	Discharge capacity [mAh/g]
SFG_1	57.5
SFG_2	47.4
SFG_3	40.7
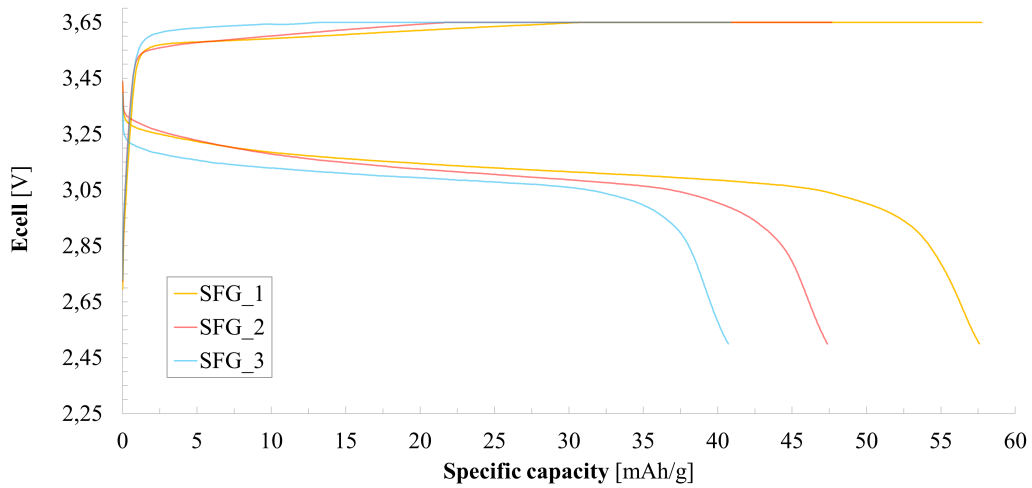
Figure 4.12: The charge/discharge curves of the first cycle at C/10 for the SFG cells. The specific discharge capacities can be read at the end of the lower discharge curve.

The rate performance through each C-rate of SFG cells is presented in Figure 4.13. The cells' exhibit poor performance across all rates. The highest capacities reached, excluding the formation step, were those during the first cycles at C/3 obtaining 9 mAh/g on average. The CE for the SFG cells are presented in Figure 4.14. The cells exhibit no consistency in CE having high standard deviations.

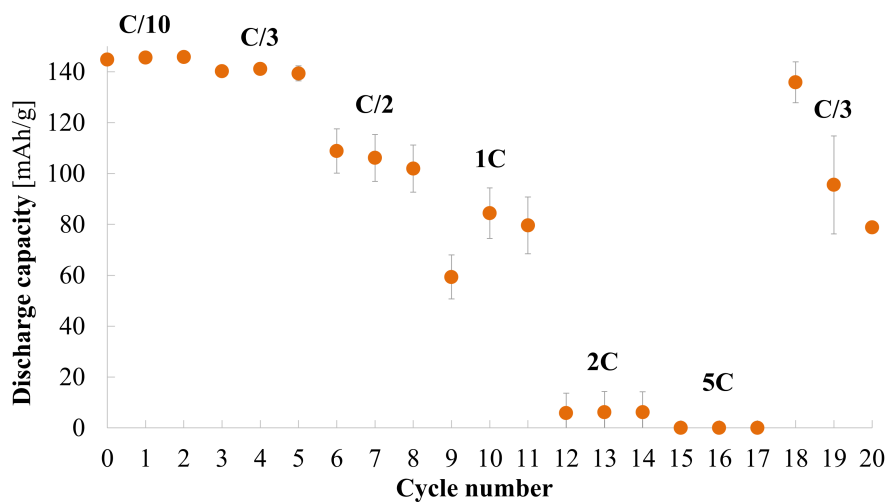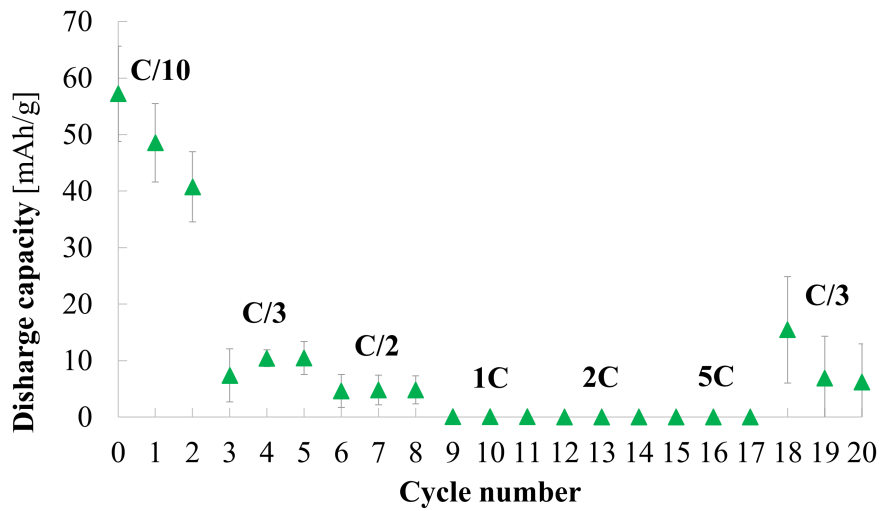**Figure 4.13:** Average rate performance results of the SFG cells. Standard deviations were derived from three cell replications.
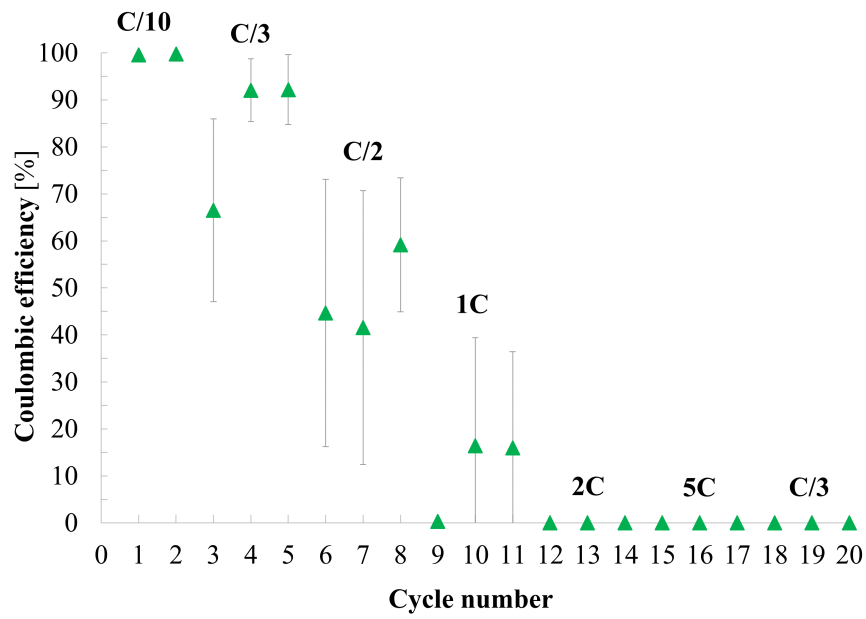
Figure 4.14: The average coulombic efficiency for the SFG cells. CE at 2C, 5C and the second C/3 step were set to 0% due to cell failure at these rates. The standard deviation was derived from three cell replications.

4.4 Carbon comparison

A comparison of rate performance between the conductive carbons is presented in Figure 4.15. As seen in the figure, SFG deviates significantly from to C45 and KB, achieving no discernible capacity values matching the other two carbons during any of rate the steps. All cell types underperform at 2C and 5C, obtaining close to 0 mAh/g. In comparison, during all rates, except the second C/3 step, KB achieved higher discharge capacities than C45. Exact values and percentiles are presented in Table 4.9. At C/10, the difference is marginal, with KB having ∼0.6% higher capacity than C45. The first C/3 step is the one step where the KB cells consistently out-performed C45. Here, the KB achieved ∼10% higher capacities than C45, on average. During C/2 and 1C, KB again performed slightly better than C45, with a average capacity of 4.5 and 5.6% higher. In the capacity retention test step at C/3, C45 achieved 4.1% higher average capacity of than KB's with comparably high standard deviation. Although all samples exhibited poor performance at 2C and 5C, C45 demonstrated slightly better performance at higher rates (2C), while KB exhibited better performance at lower rates (C/10-1C).
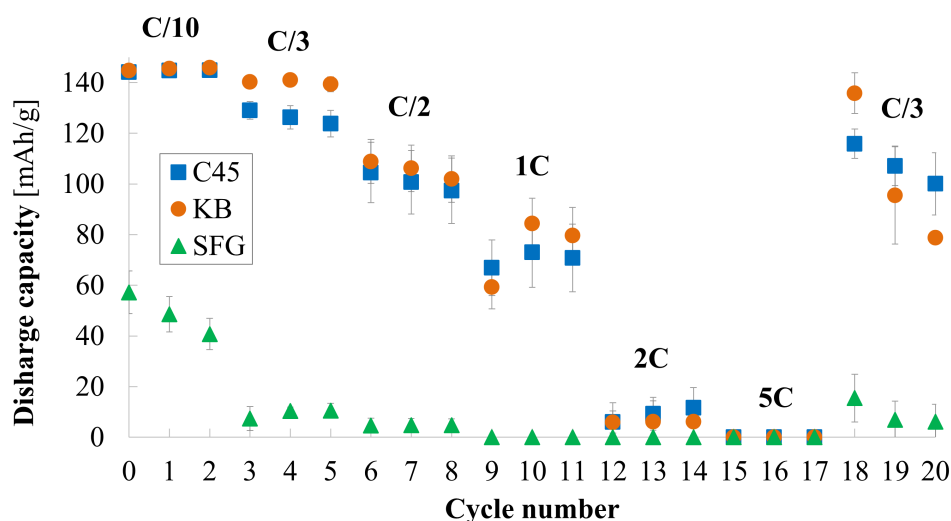
Figure 4.15: The rate performance results for the three types of cells tested. The first cycle is given at N = 0. The standard deviation is derived from three cells replicates per carbon.

Table 4.9: Each average discharge capacity for the C-rates of the C45 and KB cells, with respective standard deviations. The percentile difference is given with respect to KB.

C-rate	C45	KB	KB/C45 relation
	Average discharge capacity [mAh/g]		[%]
C/10	144.6 ± 0.3	145.4 ± 0.4	+ 0.6
C/3	126.4 ± 2.1	140.2 ± 0.7	+ 9.8
C/2	100.8 ± 2.9	105.6 ± 2.9	+ 4.5
1C	70.2 ± 2.6	74.4 ± 10.9	+ 5.6
2C	9.0 ± 2.3	6.1 ± 0.2	- 32.2
5C	0.0 ± 0.0	0.0 ± 0.0	N/A
C/3	107.7 ± 6.5	103.4 ± 23.9	- 4.1

Capacity retention (CR) was calculated with respect to the first and second c/3 rate steps, with their values listed in Table 4.10. The values for the third conductive carbon, SFG, are not included as their poor cycling performance at both C/3 steps render their CR non-applicable. The respective CE used in the calculation of CR is presented in Figure 4.16. The 2C and 5C CE are represented as values of zero because of cell failure observed at these rates. As seen in Table 4.10, C45 retains a higher capacity between the two C/3 steps than KB, with a relatively low standard deviation. With its highest value, the C45 CR nears 90%. KB obtained an average CR of ∼73%, with its highest value nearing 85%. The standard deviation of KB is more than 3 times larger than that of C45, as seen in the scattering of data points for KB during the second C/3 rate step (N = 18-20; Figure 4.15). The CE of C45 and KB match in large part during C/10, C/3 and C/2, both averaging near 98%. A small drop occurs when entering C/3 and C/2 for both. At the 1C rate step a decrease of 10% can be seen in both cell types. A significant decrease of KB occurred at N = 9, down to ∼65% CE. A similar, but smaller decrease for C45 at N = 9 also occurred. At the returning C/3 rate step both C45 and KB achieve near 98% CE. Note that N = 18, corresponding with the second C/3 step, is plotted as 0% CE in Figure 4.16.

Table 4.10: The average capacity retention (CR) between the first and second C/3 cycling step for the three cell types. Averages of three replications for each carbon is shown, with standard deviation for each replication.

Sample	CR [%]
C45	85.0 ± 4.7
KB	73.9 ± 15.6
SFG	N/A
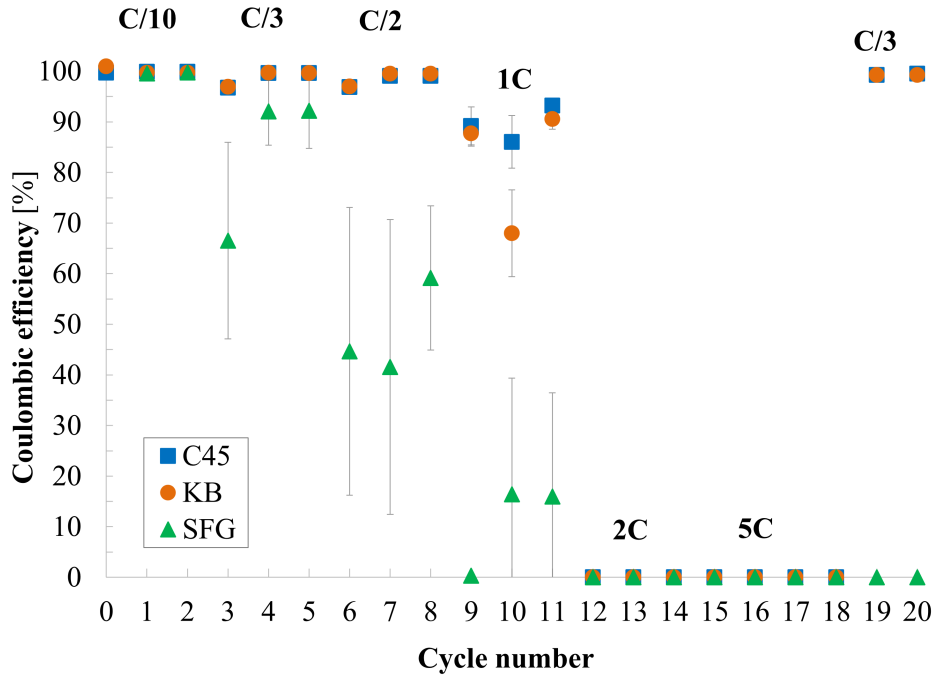
Figure 4.16: The Coulombic efficiency (CE) for the averages of the three types of cells. The averages are derived from three replications per carbon, with their standard deviations.

A total summary of all the main findings within this study is presented in Table 4.11. No standard deviations are included.

Table 4.11: Summary of test results of the three conductive carbons C45, KB and SFG.

Sample		C45	KB	SFG
BET surface area $[\text{m}^2/\text{g}]$		46	1332	9
Crystallinity		Amorphous	Highly amorphous	Highly crystalline
Solid content [%]		40	30	40
Mass loading $[\text{mg/cm}^2]$		6.3	4.5	6.6
	C/10	145	145	49
	C/3	126	140	9
	C/2	101	106	5
Discharge	1C	70	74	0
capacities $[\text{mAh/g}]$	2C	10	5	0
	5C	0	0	0
	C/3	108	103	10
Capacity retention [%]		85	74	N/A

5 Discussion

5.1 C45, KB and SFG as conductive additives

The battery cells containing the conductive carbons C45 and KB achieved comparable capacities, Coulombic efficiency and capacity retention. The SFG cells were not comparable, and performed worse at every C-rate. X. Qi et. al. found that an electrode's capacity reached its maximum for conductive additives with a surface area in the ranges of 100-200 m^2/g [21]. Therefore, as an introductory hypothesis, KB was expected to have too large of a surface area to be able to provide the conductive network needed to obtain high rate performance results compared to a more commercialised conductive additive, like C45. As the results showed, this proved to not be the case. The KB cells slightly out-performed the C45 cells in terms of rate performance. The SFG cells, on the other hand, under-performed at all rate performance metrics.

C45 and KB gave rise to quite similar rate performance results, but varied in XRD crystallinity and BET surface area. KB slightly out-performed C45 in cycling capacity at C/10, C/3, C/2 and 1C. However, the capacity retention was significantly lower, and the Coulombic efficiency was on average also lower than C45, with higher standard deviations. The surface area and morphology play an important role for the electrode conductivity, porosity and rate capability. In the aforementioned study, BET surface areas above 580 m^2/g resulted in decreasing electrode conductivity. This suggests that the high surface area of the KB particles should hinder the electrolyte transport within the electrode and thereby decrease the ionic conductivity of the battery. This would indicate that all rate performance metrics of KB should be lower than C45 because of the significant difference in surface area. The rate performance results in this study, however, do not show this. The KB aggregates, spread between the LFP particles, manage to maintain ionic conductivity in the cathode, thus matching and reaching higher capacities than C45 at the four given C-rates.

The XRD patterns of both C45 and KB indicate amorphous materials. The wide and undefined peaks are an indication of the amorphous structure of the carbons, which suggests a low structure and a low graphitic character. The randomly packed carbon aggregates likely assemble complex branching structures, like a tree's canopy. Since C45 and KB exist as amorphous carbons (with KB's diffractogram indicating a more amorphous structure), their layering with LFP in the cathode creates electrically conductive branches. Furthermore, KB and its high surface area particles, creates many contact points at the interface between LFP and the conductive additive. These contact points act as pathways for the electrons, and are dominating in determining the electronic conductivity of the electrode. With C45's lower BET surface area, the branching structure within the electrode assumably creates fewer contact points on the active particles. This yields an overall lower electronic conductivity for C45, however, the rate performance results of C45 and KB can't be explained by their electronic conductivities alone. As explained by

Wang et. al., the ionic conductivity is one of four parts determining the charge transport system within the cathode, and it is controlled by the porous structure of the cathode [16]. The less amorphous C45, with its higher structure compared to KB, may inherit more empty space between each aggregate. This could give rise to a more porous cathode composition. With a higher porosity, C45 may allow for a greater electrolyte distribution than KB, and thus an increase in ionic conductivity. With KB achieving slightly higher rate capacities, but not higher CE or CR than C45, a trade-off between electrical and ionic conductivity might have occurred due to its high surface area. The cathode containing KB may retain a high amount of electrical conductivity, but will lose this conductivity over time. This could be assumed to be the one of reasons for the lower capacity retention of the KB cells. The unexpected deviations of the KB values may indicate that the electrode is less stable and more unpredictable than C45. It is hard to point out a reason why this is the case, but the carbon's large surface area might be an important factor.

Based on the results, C45's amorphous structure and BET surface area enables both sufficient electronic and ionic pathways within the electrode. The structure creates many contact points on the surface of the LFP particles and simultaneously provides pores with high enough volume to support even electrolyte distribution. This allows for good electrical and ionic conductivity, and therefore acceptable rate performance results.

In comparison to the other electrodes, the SFG did not perform well in rate performance, both failing to achieve similar specific capacity values and to establish a stable CE at any rate step. The BET analysis showed that SFG has a surface area 0.7 times the LFP surface area, as opposed to the other two carbons with a much larger surface area. The SFG carbon also differentiates itself from the other conductive carbons in the XRD results. The diffractogram in Figure 4.1 indicates a highly crystalline graphitic structure. The aggregates of SFG form a complex layered structure, similar to graphite, and the carbons' internal electrical conductivity is comparable to that of graphite. The relatively small BET surface area of the SFG particles can be thought to create fewer contact points with LFP, reducing the electronic pathways available for the transport of electrons between the additive and the active material. This might have resulted in a high dispersion of charge and loss of energy potential during lithiation and delithiation, which devastated the overall performance of the cell. The XRD and BET results of SFG suggest that it would be better utilised as an anode material, rather than a conductive additive, due to its highly crystalline structure similar to graphite.

In summary, while SFG has good internal electrical conductivity, its low contact area with the active material particles and poor ionic conductivity prevents it from being a suitable conductive additive for LFP cathodes in this particular cell arrangement.

5.2 Cell deviations and experimental errors

All three cell types deliver close to zero capacities at 2C and 5C. Given the results, the cells simply cannot deliver enough charge carrying Li^+-ions over these durations of time. With a half-cell composition, the LFP cathodes containing the three conductive carbons C45, KB and SFG are not suitable for use at 2C or above.

During the production of the slurries and casts, it was found that the solid content of the KB-slurry had to be lowered to 30%. This is due to KB's large surface area, so more NMP is needed to fill all the pores in the particles and fully wet the powder. The difference in solid content explains why the mass loading of KB is notably lower than that of the two other types of electrode. Assuming the same volume of slurry is used for every cast, and that most of the NMP evaporates during drying, a correlation between solid content and mass loading is expected. This is supported in Table 3.3 and Figure 4.2.

The mass loading of active materials on the current collectors has a big impact on the cell's performance in terms of both charge storage and output. The variation in mass loading may therefore have affected the cycling results. Based on values from Table 3.3 alone, KB is expected to perform better than the other two electrodes. With such large variations between the mass loading values, it is hard to determine exactly how much influence the mass loading has on the performance. Thus, the concluding statements of this report must be viewed in consideration of the differences in mass loading.

During the first charge-discharge cycle of the second C/3 rate step, in cycle 18, all cell types achieved CEs over 100%. This can be seen in the individual graphs or in the graphs comparing the three carbons (Figures 4.5, 4.9, 4.13 and 4.16) where N = 18 is set to 0% CE. A reason for this may be because of accumulation of unrecovered charge, which affects the total cell capacity. This happens because high C-rates cause a larger difference between charge and discharge capacities due to accumulation of Li^+-ions that are not properly intercalated. When the cells are subjected to a discharge current at C/3 the second time, it is able to discharge the accumulated stockpile and the added charge. This results in discharge capacities much greater than their corresponding charge capacities, and CE values above 100%.

Open circuit voltage (OCV) is a fundamental parameter for estimating initial performance of the cell. The discrepancy in $C45_3$ and $C45_1$ may have occurred due to an array of different experimental errors. Every step in the manual manufacturing process of the half-cell is integral to good battery health and behaviour. A sub-optimal OCV reading may give an indication of errors during either the preparation and making of the electrodes or the assembly of the half-cells. Given that $C45_2$ gave an OCV reading of 3.4 V and that all the three cathodes where punched from the same cast with a low deviation in mass loading, it is likely that the assembly of the cell is to blame. A slight misplacement of either the anode, separator or cathode in relation to the rest of the battery components might have impacted the cell's OCV. As P. Luc et. al. details in their investigation of reproducibility in manual production of coin cells [55], to reduce the assembler's influence on reproducibility, each assembler should have experience in assembling around 50 cells before attempting main experiments. Also, the assembler within one project should not be interchanged. For the assembly of cells within this project, the same assembler was kept for all 3 cells of C45, KB and SFG. But, inexperience in coin cell making, in contrast to the suggested amount from P. Luc et. al., may have influenced not only the OCV readings, and to an extent the performance capabilities of the C45 cells, but also the accompanying results of the KB and SFG cells.

6   Conclusion

In this comparative study, the aim was to investigate and compare different carbons' effect on rate performance of LFP cathodes. A method for producing LFP cathodes, assembly of LFP coin cells and cycling were developed and tested. First, a method for making slurries for LFP cathodes was established, accompanied by solid content adjustments based on the samples' varying surface area. The higher solvent requirement for the cathode containing the KB carbon was attributed to its significant absorption capacity.

The C45 and KB carbons measured BET surface areas of 46 and 1332 m^2/g, respectively, and were from XRD analysis, found to exhibit microstructures of low crystallinity. In contrast, the SFG carbon was found to be highly crystalline and had a BET surface area of 9 m^2/g. From the rate performance testing, the C45 and KB cells obtained similar results, while the SFG cells was non-comparable with its poor overall performance. The KB cells slightly out-performed the C45 cells in the capacities achieved with increasing C-rates, but exhibited a much worse capacity retention. The discharge capacities at C/10, C/3, C/2, 1C, 2C, 5C and C/3 of the C45 cells was measured to 145, 126, 101, 70, 10, ∼0 and 107 mAh/g, respectively. The KB cells achieved 145, 140, 105, 74, 5, ∼0 and 108 mAh/g and the SFG cells obtained approximately 49, 9, 5, ∼0, ∼0, ∼0 and 10 mAh/g. Although all carbons exhibited poor performance at 2C and 5C, C45 demonstrated slightly better performance at a higher rate (2C), while KB exhibited better performance at lower rates (C/10-1C). The C45 and KB cells retained 85% and 74% of their capacity at C/3, respectively, while the SFG cells gave capacity retention results that were too low to define appropriately.

The amorphous structure of the C45 carbon might have supported an inner branching structure that would facilitate a favorable electronic and ionic conductivity within the cathode. In contrast, the KB carbon, with its higher BET surface area and greater amorphous structure, potentially facilitated an enhanced electronic conductivity, but achieved comparably lower ionic conductivity than C45. This discrepancy might be because of reduced pore volume within the cathode, limiting electrolyte distribution and impeding the flow of Li$^+$-ions. This might have resulted in the KB cells achieving overall lower capacity retention than the C45 cells. The SFG carbon on, the other hand, with its low BET surface area and highly crystalline profile, might have contributed to both poor electronic and ionic conductivity in the cathode. This could be the reason for the poor rate performance observed for the SFG cells across all metrics.

A possible error in the comparison between the conductive carbons was discussed. The mass loading difference might possibly have played a significant role in the rate performance results for the KB cells. With higher mass loading, more equal to C45 and SFG, KB might have showed lower discharge capacities than C45. The exact degree of this effect is unknown, but did create ambiguity in the carbon comparison.

To conclude, the poor cycling performance of SFG invalidates its suitability as a conductive carbon additive for LFP cathodes due to its crystalline structure. C45 makes for a good additive when it comes to cycle life, due to its higher capacity retention compared to KB, but KB slightly outperforms C45 in terms of low-rate discharge capacity.

7 Future Work

Mass loading for KB was lower than the other conductive carbons and this may have influenced the results, wrongly enhancing KB's performance. Due to its BET surface area being up to 25 times greater than C45, the solid content got reduced to obtain a more similar viscosity, which lowered the mass loading. A optimisation of the slurry formulation which could give equal mass loading, may be beneficial for further research and comparability. Carbon coated aluminium current collectors was not used in the making of the cathodes. Using such current collectors could possibly give increased discharge capacities and enable the cells to survive during high current loading rates.

For further powder characterisation and visual comparison of the carbons, particle size estimations could have been done. Methods like PSD or the use of SEM/TEM could give valuable insight into the cells inner layering with LFP and therefore give a more grounded explanation of the rate performance results.

In this study, the rate performance steps of 2C and 5C proved to be too heavy for the cell types to handle. Therefore, an adjustment of the steps could have been made, e.g. to include 1.5C and 1.75C. This could possibly have resulted in the cells not failing and therefore giving more realistic capacity retention data.

As an extension of this study, it might prove beneficially to investigate the long term cycling life of the LFP/carbon cathodes. Only rate performance was investigated in this study, with a maximum of 21 cycles. Therefore, to investigate how the carbons react after long term cycling could provide useful information in the realistic usage of the cells.

Bibliography

[1] Naoki Nitta et al. "Li-ion battery materials: present and future". In: *Materials Today* 18.5 (June 2015), pp. 252–264. ISSN: 13697021. DOI: 10.1016/j.mattod.2014.10.040. URL: https://linkinghub.elsevier.com/retrieve/pii/S1369702114004118 (visited on Mar. 23, 2023).

[2] Amato Alessia et al. "Challenges for sustainable lithium supply: A critical review". In: *Journal of Cleaner Production* 300 (June 1, 2021), p. 126954. ISSN: 0959-6526. DOI: 10.1016/j.jclepro.2021.126954. URL: https://www.sciencedirect.com/science/article/pii/S0959652621011732 (visited on May 16, 2023).

[3] Yoshio Nishi. "The development of lithium ion secondary batteries". In: *The Chemical Record* 1.5 (2001). _eprint: https://onlinelibrary.wiley.com/doi/pdf/10.1002/tcr.1024, pp. 406–413. ISSN: 1528-0691. DOI: 10.1002/tcr.1024. URL: https://onlinelibrary.wiley.com/doi/abs/10.1002/tcr.1024 (visited on May 4, 2023).

[4] Da Deng. "Li-ion batteries: basics, progress, and challenges". In: *Energy Science & Engineering* 3.5 (2015). _eprint: https://onlinelibrary.wiley.com/doi/pdf/10.1002/ese3.95, pp. 385–418. ISSN: 2050-0505. DOI: 10.1002/ese3.95. URL: https://onlinelibrary.wiley.com/doi/abs/10.1002/ese3.95 (visited on May 4, 2023).

[5] Ozan Toprakçı et al. "ChemInform Abstract: Fabrication and Electrochemical Characteristics of LiFePO4 Powders for Lithium-Ion Batteries". In: *ChemInform* 42 (Oct. 25, 2011). DOI: 10.1002/chin.201143199.

[6] Yu Miao et al. "Current Li-Ion Battery Technologies in Electric Vehicles and Opportunities for Advancements". In: *Energies* 12.6 (Jan. 2019). Number: 6 Publisher: Multidisciplinary Digital Publishing Institute, p. 1074. ISSN: 1996-1073. DOI: 10.3390/en12061074. URL: https://www.mdpi.com/1996-1073/12/6/1074 (visited on May 4, 2023).

[7] Hong Li. "Practical Evaluation of Li-Ion Batteries". In: *Joule* 3.4 (Apr. 17, 2019), pp. 911–914. ISSN: 2542-4351. DOI: 10.1016/j.joule.2019.03.028. URL: https://www.sciencedirect.com/science/article/pii/S2542435119301680 (visited on May 4, 2023).

[8] Adam Tornheim and Daniel C. O'Hanlon. "What do Coulombic Efficiency and Capacity Retention Truly Measure? A Deep Dive into Cyclable Lithium Inventory, Limitation Type, and Redox Side Reactions". In: *Journal of The Electrochemical Society* 167.11 (July 2020). Publisher: IOP Publishing, p. 110520. ISSN: 1945-7111. DOI: 10.1149/1945-7111/ab9ee8. URL: https://dx.doi.org/10.1149/1945-7111/ab9ee8 (visited on May 4, 2023).

[9] Jie Xiao et al. "Understanding and applying coulombic efficiency in lithium metal batteries". In: *Nature Energy* 5.8 (Aug. 2020). Number: 8 Publisher: Nature Publishing Group, pp. 561–568. ISSN: 2058-7546. DOI: 10.1038/s41560-020-0648-z. URL: https://www.nature.com/articles/s41560-020-0648-z (visited on May 11, 2023).

[10] K. Mizushima et al. "LixCoO2: A NEW CATHODE MATERIAL FOR BATTERIES OF HIGH ENERGY DENSITY". In: *Materials Research Bulletin* 15.6 (June 1, 1980), pp. 783–789. ISSN: 0025-5408. DOI: 10.1016/0025-5408(80)90012-4. URL: https://www.sciencedirect.com/science/article/pii/0025540880900124 (visited on May 16, 2023).

[11] Gaizka Saldaña et al. "Analysis of the Current Electric Battery Models for Electric Vehicle Simulation". In: *Energies* 12 (July 18, 2019), p. 2750. DOI: 10.3390/en12142750.

[12] Koichi Momma and Fujio Izumi. "ıt VESTA3 for three-dimensional visualization of crystal, volumetric and morphology data". In: *Journal of Applied Crystallography* 44.6 (Dec. 2011), pp. 1272–1276. DOI: 10.1107/S0021889811038970. URL: https://doi.org/10.1107/S0021889811038970.

[13] Wontae Lee et al. "Advances in the Cathode Materials for Lithium Rechargeable Batteries". In: *Angewandte Chemie International Edition* 59.7 (2020), pp. 2578–2605. ISSN: 1521-3773. DOI: 10.1002/anie.201902359. URL: https://onlinelibrary.wiley.com/doi/abs/10.1002/anie.201902359 (visited on Apr. 14, 2023).

[14] Jordi Cabana et al. "Beyond Intercalation-Based Li-Ion Batteries: The State of the Art and Challenges of Electrode Materials Reacting Through Conversion Reactions". In: *Advanced Materials* 22.35 (2010). _eprint: https://onlinelibrary.wiley.com/doi/pdf/10.1002/adma.201000717, E170–E192. ISSN: 1521-4095. DOI: 10.1002/adma.201000717. URL: https://onlinelibrary.wiley.com/doi/abs/10.1002/adma.201000717 (visited on May 3, 2023).

[15] Junbo Hou et al. "Materials and electrode engineering of high capacity anodes in lithium ion batteries". In: *Journal of Power Sources* 450 (Feb. 29, 2020), p. 227697. ISSN: 0378-7753. DOI: 10.1016/j.jpowsour.2019.227697. URL: https://www.sciencedirect.com/science/article/pii/S0378775319316908 (visited on Apr. 27, 2023).

[16] Yu Wang et al. "Strategies for Building Robust Traffic Networks in Advanced Energy Storage Devices: A Focus on Composite Electrodes". In: *Advanced Materials* 31.6 (2019). _eprint: https://onlinelibrary.wiley.com/doi/pdf/10.1002/adma.201804204, p. 1804204. ISSN: 1521-4095. DOI: 10.1002/adma.201804204. URL: https://onlinelibrary.wiley.com/doi/abs/10.1002/adma.201804204 (visited on Apr. 27, 2023).

[17] Karim Zaghib et al. "Effect of carbon source as additives in LiFePO4 as positive electrode for lithium-ion batteries". In: *Electrochemical and Solid State Letters - ELECTROCHEM SOLID STATE LETT* 8 (Jan. 1, 2005). DOI: 10.1149/1.1865652.

[18] Dana Pantea et al. "Electrical conductivity of conductive carbon blacks: Influence of surface chemistry and topology". In: *Applied Surface Science* 217 (July 1, 2003), pp. 181–193. DOI: 10.1016/S0169-4332(03)00550-6.

[19] J. Lahaye and F. Ehrburger-Dolle. "Mechanisms of carbon black formation. Correlation with the morphology of aggregates". In: *Carbon* 32.7 (Jan. 1, 1994), pp. 1319–1324. ISSN:

0008-6223. DOI: 10.1016/0008-6223(94)90118-X. URL: https://www.sciencedirect.com/science/article/pii/000862239490118X (visited on Apr. 14, 2023).

[20] Jean-Baptiste Donnet, Roop Chand Bansal, and Meng-Jiao Wang, eds. *Carbon black: science and technology*. 2nd ed., rev. and expanded. p. 110-111. New York: Dekker, 1993. 461 pp. ISBN: 978-0-8247-8975-6.

[21] Xin Qi et al. "Understanding the influence of conductive carbon additives surface area on the rate performance of LiFePO4 cathodes for lithium ion batteries". In: *Carbon* 64 (Nov. 1, 2013), pp. 334–340. ISSN: 0008-6223. DOI: 10.1016/j.carbon.2013.07.083. URL: https://www.sciencedirect.com/science/article/pii/S0008622313007173 (visited on Apr. 14, 2023).

[22] Núria Tricàs Rosell. "Plasma modification on carbon black surface: From reactor design to final applications". Accepted: 2011-04-12T18:39:56Z Publication Title: TDX (Tesis Doctorals en Xarxa). PhD thesis. Universitat Ramon Llull, June 1, 2007. URL: https://www.tdx.cat/handle/10803/9288 (visited on Apr. 14, 2023).

[23] Jay Janzen and Gerard Kraus. "Specific Surface Area Measurements on Carbon Black". In: *Rubber Chemistry and Technology* 44.5 (Nov. 1, 1971), pp. 1287–1296. ISSN: 0035-9475. DOI: 10.5254/1.3544809. URL: https://doi.org/10.5254/1.3544809 (visited on Apr. 14, 2023).

[24] Kim Kinoshita. *Carbon: Electrochemical and physicochemical properties*. p. 110-111. New York: John Wiley & Sons, 1988. 533 pp. ISBN: 0-471-84802-6.

[25] Godfrey Sikha, Branko Popov, and Ralph White. "Effect of Porosity on the Capacity Fade of a Lithium-Ion Battery Theory". In: *Journal of The Electrochemical Society - J ELECTROCHEM SOC* 151 (July 1, 2004). DOI: 10.1149/1.1759972.

[26] *Slurry definition and meaning — Collins English Dictionary*. May 2, 2023. URL: https://www.collinsdictionary.com/dictionary/english/slurry (visited on May 2, 2023).

[27] Jianlin Li et al. "From Materials to Cell: State-of-the-Art and Prospective Technologies for Lithium-Ion Battery Electrode Processing". In: *Chemical Reviews* 122.1 (Jan. 12, 2022), pp. 903–956. ISSN: 0009-2665, 1520-6890. DOI: 10.1021/acs.chemrev.1c00565. URL: https://pubs.acs.org/doi/10.1021/acs.chemrev.1c00565 (visited on Apr. 17, 2023).

[28] *Polyvinylidene Fluoride (PVDF) - Material Properties & Other Info*. URL: https://omnexus.specialchem.com/selection-guide/polyvinylidene-fluoride-pvdf-plastic (visited on May 2, 2023).

[29] James Sherwood, Thomas Farmer, and James Clark. "Catalyst: Possible Consequences of the N-Methyl Pyrrolidone REACH Restriction". In: *Chem* 4 (Sept. 1, 2018), pp. 2010–2012. DOI: 10.1016/j.chempr.2018.08.035.

[30] J. B. Goodenough. "Battery Components, Active Materials for". In: *Batteries for Sustainability: Selected Entries from the Encyclopedia of Sustainability Science and Technology.* Ed. by Ralph J. Brodd. New York, NY: Springer, 2013, pp. 51–92. ISBN: 978-1-4614-5791-6. DOI: 10.1007/978-1-4614-5791-6_3. URL: https://doi.org/10.1007/978-1-4614-5791-6_3 (visited on May 7, 2023).

[31] Yujin Kim et al. "Investigation of mass loading of cathode materials for high energy lithium-ion batteries". In: *Electrochemistry Communications* 147 (Feb. 1, 2023), p. 107437. ISSN: 1388-2481. DOI: 10.1016/j.elecom.2023.107437. URL: https://www.sciencedirect.com/science/article/pii/S1388248123000115 (visited on May 4, 2023).

[32] Honghe Zheng et al. "A comprehensive understanding of electrode thickness effects on the electrochemical performances of Li-ion battery cathodes". In: *Electrochimica Acta* 71 (June 1, 2012), pp. 258–265. ISSN: 0013-4686. DOI: 10.1016/j.electacta.2012.03.161. URL: https://www.sciencedirect.com/science/article/pii/S0013468612005270 (visited on May 7, 2023).

[33] Junfei Liang et al. "Ultra-High Areal Capacity Realized in Three-Dimensional Holey Graphene/SnO2 Composite Anodes". In: *iScience* 19 (Aug. 1, 2019). DOI: 10.1016/j.isci.2019.08.025.

[34] Madhav Singh, Jörg Kaiser, and Horst Hahn. "Thick Electrodes for High Energy Lithium Ion Batteries". In: *Journal of The Electrochemical Society* 162.7 (Apr. 1, 2015). Publisher: IOP Publishing, A1196. ISSN: 1945-7111. DOI: 10.1149/2.0401507jes. URL: https://iopscience.iop.org/article/10.1149/2.0401507jes/meta (visited on Apr. 17, 2023).

[35] Zhifu Liu, Yiling Wang, and Yongxiang Li. "Combinatorial Study of Ceramic Tape-Casting Slurries". In: *ACS Combinatorial Science* 14.3 (Mar. 12, 2012), pp. 205–210. ISSN: 2156-8952, 2156-8944. DOI: 10.1021/co200148q. URL: https://pubs.acs.org/doi/10.1021/co200148q (visited on Apr. 17, 2023).

[36] Ben Rowden and Nuria Garcia-Araez. "Estimating lithium-ion battery behavior from half-cell data". In: *Energy Reports* 7 (May 1, 2021), pp. 97–103. DOI: 10.1016/j.egyr.2021.02.048.

[37] M Braun. *Glove Box Systems Gas purification platform MB20/MB200 and Labmaster SP/DP Operating Manual.* URL: https://seabaugh.nd.edu/assets/330934/at_man_mbraunglobebox_mb20_200_lmsp_dp_std_en.pdf.

[38] C. J. Barton. *A Review of Glove Box Construction and Experimentation.* Google-Books-ID: 9ie90I1BndwC. Oak Ridge National Laboratory, 1961. 118 pp.

[39] Vivian Murray, David Hall, and J Dahn. "A Guide to Full Coin Cell Making for Academic Researchers". In: *Journal of The Electrochemical Society* 166 (Jan. 30, 2019), A329–A333. DOI: 10.1149/2.1171902jes.

[40] Fang Dai and Mei Cai. "Best practices in lithium battery cell preparation and evaluation". In: *Communications Materials* 3.1 (Sept. 9, 2022). Number: 1 Publisher: Nature Publishing Group, pp. 1–6. ISSN: 2662-4443. DOI: 10.1038/s43246-022-00286-8. URL: https://www.nature.com/articles/s43246-022-00286-8 (visited on Apr. 17, 2023).

[41] Elahe Talaie et al. "Methods and Protocols for Electrochemical Energy Storage Materials Research". In: *Chemistry of Materials* 29.1 (Jan. 10, 2017). Publisher: American Chemical Society, pp. 90–105. ISSN: 0897-4756. DOI: 10.1021/acs.chemmater.6b02726. URL: https://doi.org/10.1021/acs.chemmater.6b02726 (visited on Apr. 20, 2023).

[42] *IEC 60086-3:2021 — IEC Webstore*. URL: https://webstore.iec.ch/publication/63418 (visited on Apr. 17, 2023).

[43] Christopher J. Orendorff. "The Role of Separators in Lithium-Ion Cell Safety". In: *The Electrochemical Society Interface* 21.2 (Jan. 1, 2012). Publisher: IOP Publishing, p. 61. ISSN: 1944-8783. DOI: 10.1149/2.F07122if. URL: https://iopscience.iop.org/article/10.1149/2.F07122if/meta (visited on Apr. 17, 2023).

[44] Isidor Buchmann. *Batteries in a portable world: A Handbook on Rechargeable Batteries for Non-engineers*. 4th ed. Canada: Cadex Electronics Inc., 2016. ISBN: 978-0-9682118-4-7.

[45] Nina Hwang and Andrew R. Barron. *BET Surface Area Analysis of Nanoparticles*. May 8, 2011. (Visited on Mar. 28, 2023).

[46] *BET Theory :: Anton Paar Wiki*. Anton Paar. URL: https://wiki.anton-paar.com/de-de/bet-theorie/ (visited on Apr. 27, 2023).

[47] *X-Ray diffractometer and its various component parts for X-Ray studies*. xrd.co. June 11, 2016. URL: https://xrd.co/component-parts-x-ray-diffractometer/ (visited on Apr. 27, 2023).

[48] *Bragg's law*. URL: https://www.doitpoms.ac.uk/tlplib/xray-diffraction/bragg.php (visited on Apr. 27, 2023).

[49] "Protocols for studying intercalation electrodes materials : Part I: Galvanostatic cycling with potential limitation (GCPL)". In: (Jan. 2005). URL: https://www.google.com/url?sa=t&rct=j&q=&esrc=s&source=web&cd=&cad=rja&uact=8&ved=2ahUKEwiE9YDfntb-AhVTS_EDHfY0CdYQFnoECAgQAQ&url=https%3A%2F%2Fwww.biologic.net%2Fwp-content%2Fuploads%2F2019%2F08%2Fgitt_electrochemistry-battery-an1.pdf&usg=AOvVaw06kMfhA6z4ELRsbT7C9Nns.

[50] "Protocols for studying intercalation electrodes materials: Part II: Potentiodynamic Cycling with Galvanostatic Acceleration (PCGA)". In: (Jan. 2005). URL: https://www.google.com/url?sa=t&rct=j&q=&esrc=s&source=web&cd=&ved=2ahUKEwiml9qhntb-AhXmQ_EDHZ0KBf0QFnoECAsQAQ&url=https%3A%2F%2Fwww.biologic.net%2Fwp-content%2Fuploads%2F2019%2F08%2Fpitt_electrochemistry-battery-an2.pdf&usg=AOvVaw0K9vD6Uh-MOjhLfvV3YsjP.

[51] Ed Brorein. *Lithium-Ion Cell Charging and Discharging During Life Cycle Testing Versus Formation — Keysight Blogs*. URL: https://www.keysight.com/blogs/tech/bench/2022/08/30/lithium-ion-cell-charging-and-discharging-during-life-cycle-testing-versus-formation (visited on Apr. 27, 2023).

[52] *EC-Lab software Techniques and Applications*. Version 10.38. Aug. 2014. URL: https://mmrc.caltech.edu/BioLogic%20Echem/ECLab%20Manuals/EC-Lab%20software%20Techniques%20and%20Applications%20manual.pdf.

[53] D. E. Nixon, G. S. Parry, and Alfred Rene Jean Paul Ubbelohde. "Order-disorder transformations in graphite nitrates". In: *Proceedings of the Royal Society of London. Series A. Mathematical and Physical Sciences* 291.1426 (Jan. 1997). Publisher: Royal Society, pp. 324–339. DOI: 10.1098/rspa.1966.0098. URL: https://royalsocietypublishing.org/doi/10.1098/rspa.1966.0098 (visited on Apr. 20, 2023).

[54] Sergio Federico Mayer et al. "Nitridation effect on lithium iron phosphate cathode for rechargeable batteries". In: *RSC Advances* 12.6 (Jan. 24, 2022). Publisher: The Royal Society of Chemistry, pp. 3696–3707. ISSN: 2046-2069. DOI: 10.1039/D1RA07574H. URL: https://pubs.rsc.org/en/content/articlelanding/2022/ra/d1ra07574h (visited on Apr. 20, 2023).

[55] Paul-Martin Luc, Simon Bauer, and Julia Kowal. "Reproducible Production of Lithium-Ion Coin Cells". In: *Energies* 15.21 (Jan. 2022). Number: 21 Publisher: Multidisciplinary Digital Publishing Institute, p. 7949. ISSN: 1996-1073. DOI: 10.3390/en15217949. URL: https://www.mdpi.com/1996-1073/15/21/7949 (visited on May 1, 2023).

Appendix

A   Risk Assessment

Institute:	Department of Materials Science and Engineering		Date created:	27.01.2023
Responsible faculty leader (name):	Ida Westermann		Last revised:	07.02.2023
Responsible for activities which are getting risk assessed (name):	Ivar Sande, Simen Navestad, Oscar Langfoss			
Participants (name):	Ivar Sande, Simen Navestad, Oscar Langfoss			
Description of activity, area, mv.:				

The risk assesment contains multiple activities which connects with a bachelor thesis,
where the overall activity is to test different types of carbon cathode materials and their properties.

Activity/Samples	Possible accidents	Existing risk reducing measures	Probability (P) (1-5)	Impact of consequences (I)				Risk value (P x I)	Proposal for preventative and/or corrective measures	Risk after measures (P x I)
				Human (1-5)	Materials (1-5)	Environment (1-5)	Reputation (1-5)			
NMP	Spill on ground	Use of absorption pads, waste must be thrown in separate enclosed bin under fume hood	3	1	2			4,5	Be careful when measuring NMP and work under a fume hood	2
	Skin exposure	Use of gloves and lab coat	2	2				2		
	Inhalation	Work with the chemical under a fume hood	3	2				3		
	Eye exposure	Use of protective eyewear	2	2				2		
	Health/Environment hazard	Ensure proper disposal of the chemical, clean used equipment with ethanol or isopropanol to dissolve chemical	3	1	2			4,5	Use the chamical with care and remind each other to carefully dispose of it	2
PVDF	Ingestion	No eating allowed in the lab	1	2				1		
	Skin exposure	Use of gloves and lab coat	2	2				2		
Conductive carbon	Inhalation	Work with the powder under ventilation or fume hood	4	2				4	Be careful during transportation of the material	2
	Eye exposure	Use of protective eyewear	1	1				0,5		
	Ingestion	No eating allowed in the lab	1	1				0,5		
	Skin exposure	Use of gloves and lab coat	1	1				0,5		
	Health/Environment hazard	Ensure proper disposal of the chemical, clean used equipment with ethanol or isopropanol to dissolve chemical	2	2	1			3		
Glovebox	Oxygen in the chamber	Remember to evacuate and follow the evacuation instructions	1		4			2		
	Hole in glove(s) or general leakage	Use cotton gloves inside gloves and another layer of gloves on top on that to ensure protection against corrosive substances, also check the oxygen levels inside the glovebox to check for leakage	1	1	4			2,5		
	Spill inside glovebox	Being careful with samples, use pipett	3		1			1,5		
	Damage to entrance hatch	Not tighten too much, might damage o-ring. Follow closing-instructions.	2		2			2		
Oven	Burn skin	Use of protective gloves	2	2				2		
	Drop hot sample	Use of protective gloves with grip	2	1	1			2		
XRD	Exposure to radioactivity	Students will not operate the instrument	1	2				1		
	Eye exposure of powder	Use of protective eyewear	1	2				1		
	Inhalation of powder	Careful when preparing samples	2	2				2		
BET	Spill liquid nitrogen on skin or floor	Big, stable holder for nitrogen flask	2	2				2		
	Top of nitrogen flask exploding	No use of cover on nitrogen flask	2	3	3			6	Do not fasten the lid nor point a closed container towards another person	1
	Inhalation of powder	Careful when preparing samples	1	1				0,5		
	Eye exposure of powder	Use of protective eyewear	1	2				1		
Potensiostat	Batteries heating up	Machine is placed in a seperate room	2	1				1		
Weighing	Spill on scale	Be mindful and careful, prepare waste disposial bag	3	1	1			3		
	Skin and eye exposure	Use protective gloves and eyewear	1	2				1		
	Inhalation of gasses and/or powder	Work under fume hood	2	2				2		

Figure A.1: Risk assessment

B   Additional cycling data

B.1   Calculated C-rates for C45

Table B.1: Average mAh value for each C-rate and current limit used for the C45 half-cells.

C-rate	Average [mAh]	Current limit [mAh]
C/10	0.122	0.036
C/3	0.405	0.122
C/2	0.608	0.182
1C	1.215	0.365
2C	2.431	0.729
5C	6.077	1.823

B.2   Calculated C-rates for KB

Table B.2: Average mAh value for each C-rate and current limit used for the KB half-cells.

C-rate	Average [mAh]	Current limit [mAh]
C/10	0.087	0.027
C/3	0.289	0.087
C/2	0.434	0.130
1C	0.868	0.260
2C	1.736	0.521
5C	4.340	1.302

B.3   Calculated C-rates for SFG

Table B.3: Average mAh value for each C-rate and current limit used for the SFG half-cells.

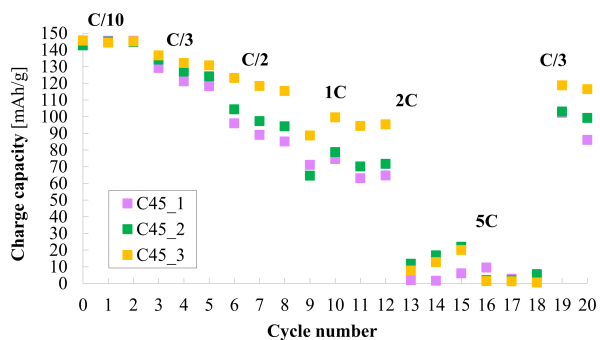| C-rate	Average [mAh]	Current limit [mAh]
C/10	0.126	0.038
C/3	0.420	0.126
C/2	0.631	0.189
1C	1.261	0.378
2C	2.523	0.757
5C	6.307	1.892

C Complimentary cycling results

C.1 C45

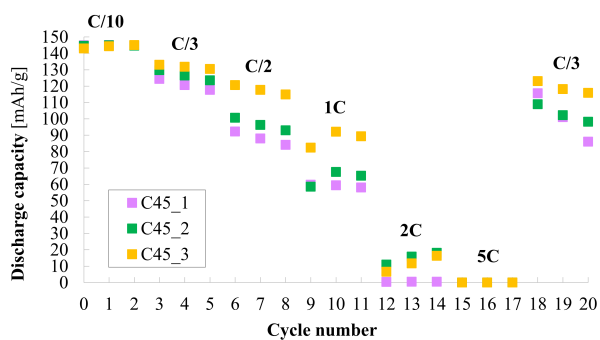**Figure C.1:** The charge capacities for each C45 cell tested.

Figure C.2: The discharge capacities for each C45 cell tested.
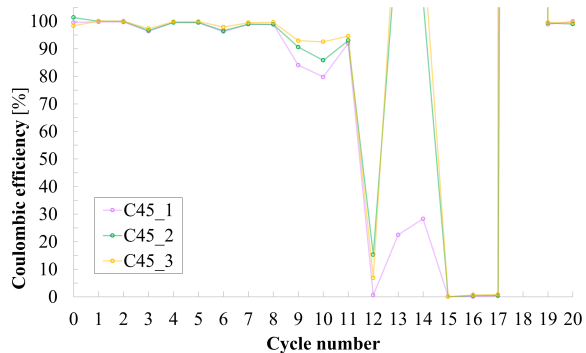

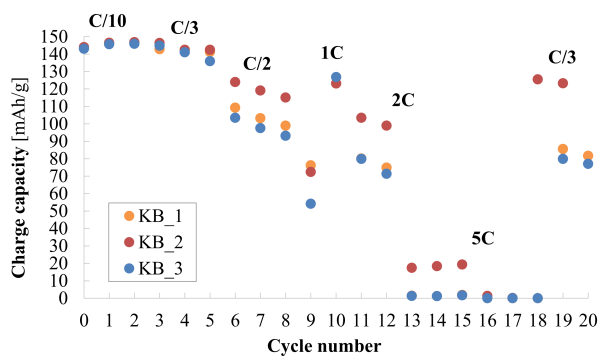**Figure C.3:** The Coulombic efficiencies for each C45 cell tested.

C.2   KB

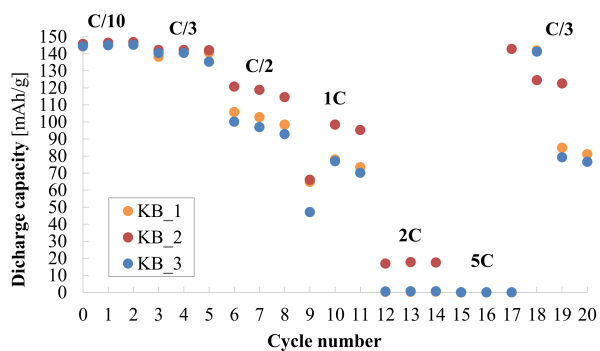**Figure C.4:** The charge capacities for each KB cell tested.

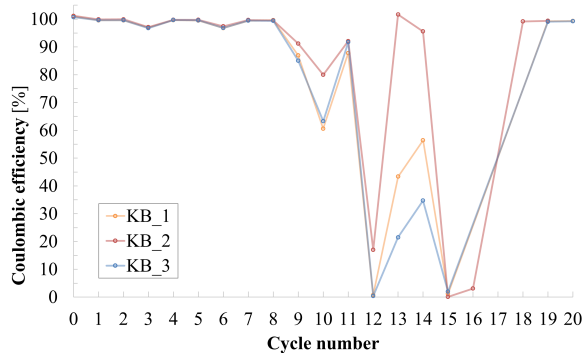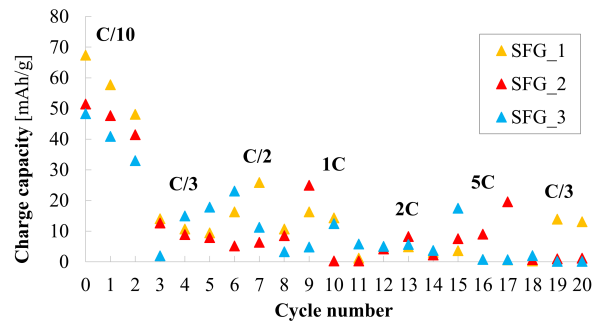**Figure C.5:** The discharge capacities for each KB cell tested.

Figure C.6: The Coulombic efficiencies for each KB cell tested.

C.3 SFG

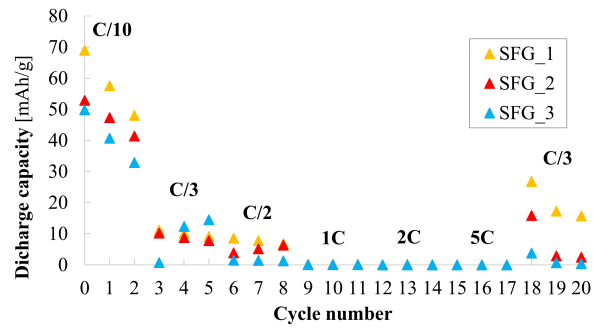**Figure C.7:** The charge capacities for each SFG cell tested.

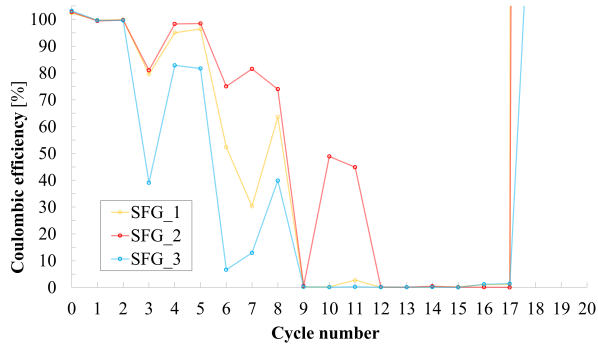**Figure C.8:** The discharge capacities for each SFG cell tested.

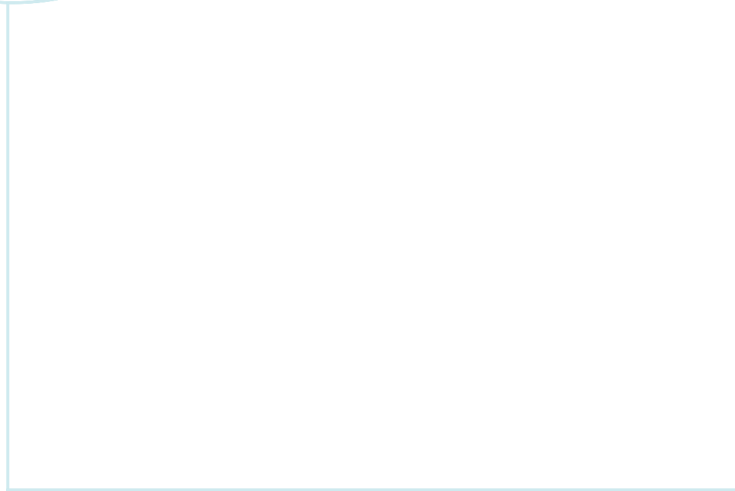**Figure C.9:** The Coulombic efficiencies for each SFG cell tested.